Cell Reports
Medicine

Article

Macrophage efferocytosis mediated by the TP63-RAC2 pathway promotes immunosuppressive remodeling in esophageal cancer

Highlights

- A pro-tumoral FN1+ macrophage subset exhibits high efferocytosis in ESCC
- TP63 transcriptionally activates RAC2 to potentiate macrophage efferocytosis
- TP63-RAC2-mediated efferocytosis drives M2 polarization of macrophages
- Targeting the TP63-RAC2 axis suppresses efferocytosis and tumor growth

Authors

Yong Xi, Zhijie Zhao, Yundong Zhou, ..., João Conde, Shiyuan Liu, Weiyu Shen

Correspondence

hongsen414@pku.edu.cn (S.H.), ndyfy02006@ncu.edu.cn (B.Y.), joao.conde@nms.unl.pt (J.C.), liushiyuan@xjtu.edu.cn (S.L.), shenweiyu@nbu.edu.cn (W.S.)

In brief

Xi et al. identify an FN1+ macrophage subtype in esophageal cancer with high efferocytosis activity. They delineate a TP63-RAC2 transcriptional axis that drives this process, promoting M2 macrophage polarization and immunosuppression. Targeting this pathway impairs efferocytosis and suppresses tumor growth, revealing a therapeutic vulnerability.

Xi et al., 2026, Cell Reports Medicine 7, 102529
January 20, 2026
https://doi.org/10.1016/j.xcrm.2025.102529

CellPress

Cell Reports Medicine

CellPress
OPEN ACCESS

Article

Macrophage efferocytosis mediated by the TP63-RAC2 pathway promotes immunosuppressive remodeling in esophageal cancer

Yong Xi,[1,2,14] Zhijie Zhao,[4,14] Yundong Zhou,[2,7,14] Chengliang Yin,[9,14] Yuxin Li,[11] Xiao Xu,[12] Wenyi Jin,[5,6] Chengbin Lin,[2] Kui Zhao,[10] Junjie Kuang,[13] Senlian Hong,[11,*] Bentong Yu,[1,*] João Conde,[8,*] Shiyuan Liu,[3,*] and Weiyu Shen[2,15,*]

[1]Department of Thoracic Surgery, the First Affiliated Hospital of Nanchang University, Nanchang, Jiangxi 330006, China
[2]Department of Thoracic Surgery, Ningbo Medical Center Lihuili Hospital, Ningbo University, Ningbo, Zhejiang 315040, China
[3]Department of Thoracic Surgery, the Second Affiliated Hospital of Xi'an Jiaotong University, Xi'an 710004, Shaanxi, China
[4]Department of Plastic and Reconstructive Surgery, Shanghai Ninth People's Hospital, Shanghai Jiao Tong University School of Medicine, Shanghai 200011, China
[5]Department of Orthopedics, Renmin Hospital of Wuhan University, Wuhan University, Wuchang, Wuhan 430060, China
[6]Department of Biomedical Sciences, City University of Hong Kong, Kowloon Tong, Hong Kong SAR 999077, China
[7]The Second Department of Oncology, Cancer Center, Huizhou First Hospital, Huizhou, Guangdong, China
[8]Comprehensive Health Research Centre (CHRC), NOVA Medical School, Faculdade de Ciências Médicas, NMS|FCM, Universidade NOVA de Lisboa, Lisboa, Portugal
[9]Department of Biomedical Engineering, Faculty of Engineering, Universiti Malaya, Kuala Lumpur, Malaysia
[10]School of Nursing, Yunnan University of Chinese Medicine, Kunming, Yunnan 650500, China
[11]State Key Laboratory of Natural and Biomimetic Drugs, Chemical Biology Center, Department of Chemical Biology, School of Pharmaceutical Sciences, Peking University, Beijing 100191, China
[12]Department of Obstetrics and Gynecology, Zhongshan Hospital, Fudan University, Shanghai, China
[13]Department of Oncology, Liuzhou People's Hospital, Guangxi Medical University, No. 8, Wenchang Road, Chengzhong District, Liuzhou, Guangxi, China
[14]These authors contributed equally
[15]Lead contact
*Correspondence: hongsen414@pku.edu.cn (S.H.), ndyfy02006@ncu.edu.cn (B.Y.), joao.conde@nms.unl.pt (J.C.), liushiyuan@xjtu.edu.cn (S.L.), shenweiyu@nbu.edu.cn (W.S.)
https://doi.org/10.1016/j.xcrm.2025.102529

SUMMARY

This study explores the role of efferocytosis in esophageal squamous cell carcinoma (ESCC) using single-cell RNA sequencing and *in vitro*/*in vivo* assays. Analyzing 27 samples from 9 patients with ESCC, we identify diverse cell types and significant heterogeneity in the tumor microenvironment, with a focus on efferocytosis. Our findings highlight that macrophages engulf apoptotic tumor cells, thereby impairing immune responses and promoting tumor progression. Notably, TP63 and RAC2 emerge as key regulators of this process, influencing efferocytosis and immune modulation. Functional assays demonstrate that disrupting these pathways alters macrophage efferocytosis and impacts tumor growth *in vivo*. These results suggest that targeting efferocytosis pathways offers potential therapeutic strategies for ESCC, enhancing antitumor immunity and improving patient outcomes. The study underscores the complex interactions between tumor cells and the immune system, with efferocytosis representing a promising therapeutic target.

INTRODUCTION

Esophageal squamous cell carcinoma (ESCC) is a highly aggressive malignancy with a poor prognosis, making it one of the leading causes of cancer-related mortality worldwide.[1–3] Despite advancements in diagnosis and treatment, the survival rate for ESCC remains dismal, as most patients are diagnosed at advanced stages when therapeutic options are limited and less effective.[4] This highlights an urgent need for innovative therapeutic strategies that target not just the tumor cells but also the tumor microenvironment (TME), a critical component of cancer progression and immune resistance.

Efferocytosis, the process by which macrophages engulf and remove apoptotic cells (ACs), plays a crucial role in maintaining tissue homeostasis and in modulating immune responses.[5,6] In the context of the TME, efferocytosis becomes a double-edged sword. While it helps clear apoptotic tumor cells, it also promotes an immunosuppressive environment by polarizing tumor-associated macrophages (TAMs) toward a tumor-promoting M2 phenotype.[7–9] This phenotype supports

tumor growth, angiogenesis, and immune evasion, creating a formidable barrier to effective antitumor immunity. Thus, understanding the mechanisms and regulatory pathways of efferocytosis in ESCC may uncover therapeutic targets to transform TAMs from tumor promoters into tumor suppressors.

ESCC, a highly aggressive and lethal malignancy, epitomizes the urgent need for deeper exploration of the TME to unravel therapeutic targets and improve patient outcomes.[10] Recent advances in single-cell RNA sequencing (scRNA-seq) have revolutionized cancer research, offering unparalleled resolution to explore cellular heterogeneity within the TME.[11,12] This approach allows for a detailed characterization of TAM subtypes, their differentiation trajectories, and their functional states, offering insights into their roles in the immunosuppressive environment of ESCC.[13] The investigation of TAM heterogeneity is particularly relevant in the context of developing targeted therapies that could modulate the TME to enhance the efficacy of existing treatments, such as immunotherapy.[14]

In this study, we leveraged scRNA-seq and a suite of experimental approaches to investigate the role of efferocytosis in ESCC. Our focus was on TAMs and their diverse roles within the immunosuppressive milieu of ESCC. By integrating gene expression, regulon activity, and differentiation pathways, we constructed a comprehensive map of TAM heterogeneity and identified key molecular drivers, including TP63 and RAC2, that regulate efferocytosis. This work not only advances our understanding of TAM function in ESCC but also highlights potential therapeutic strategies to improve patient outcomes by targeting efferocytosis pathways.

RESULTS

scRNA-seq reveals the ESCC transcriptome landscape

To ascertain the ecological microlandscape of ESCC and unveil its heterogeneity, we procured tumor tissue specimens and two sets of paired lymph node (LN) samples from nine patients with recently diagnosed ESCC devoid of any prior therapeutic interventions. The specific clinical and pathological data are presented in Table S1. We performed scRNA-seq on the 27 samples. After quality control and cell filtration, 121,038 high-quality cells were finally retained (Figures S1A–S1C and 1). As shown in Figures 1A and 1B, we identified 36 different cell clusters. Utilizing the expression levels of characteristic genes for specific cell types, these 36 cell clusters were further identified as nine distinct cell types, as illustrated in Figures 1C, 1D, and 1G. These cell types include B cells and plasma cells (IGHG1$^+$), endothelial cells (GNG11$^+$), epithelial cells (KRT14$^+$), fibroblasts (COL1A2$^+$), mast cells (TPSAB1$^+$), myeloid cells (LYZ$^+$), natural killer (NK) cells (NKG7$^+$), plasmacytoid dendritic cells (DCs) (GZMB$^+$), and T cells (CD3D$^+$). The distribution of distinct cell types across various samples is illustrated in Figures 1E and 1F. Even in the same patient, there was still high heterogeneity in the distribution of cells between different sites. As a matter of course, even if the samples were taken from the same site, the main cell subtypes were not exactly the same among different patients. Among them, the proportion of epithelial cells was the highest in tumor tissues, followed by myeloid cells, and there was higher immune cell infiltration in LNs, including B, plasma, and T cells. Moreover, the epithelial cells exhibited the highest level of proliferative activity, as shown in Figures 1H and 1I.

Heterogeneity of ESCC tumor cells

Using scRNA-seq data, we attempted to dissect the diversity and intricacy of the ESCC ecosystem at various cellular levels. Initially, we visualized the heterogeneity of the tumor cells, T cells, and macrophages.

Tumor cells were categorized into six distinct subtypes, as illustrated in Figures S2A, S2D, and S2E. Notably, C2 EZH2$^+$ tumor cells and C3 CENPF$^+$ tumor cells primarily originated from within the tumor tissues and exhibited heightened proliferative activity (Figures S2B, S2C, and S2F). Differential gene and enrichment analysis of different tumor cell subtypes showed that in C2 EZH2$^+$ tumor cells and C3 CENPF$^+$ tumor cells, DNA replication and mitosis pathways were enriched (Figures S3A–S3E). This explains the high proliferative characteristics of C2 EZH2$^+$ tumor cells and C3 CENPF$^+$ tumor cells. When tumor cells actively proliferate, their tissue differentiation ability gradually decreases. Consequently, subsequent slingshot analysis revealed that the C2 EZH2$^+$ tumor cells and C3 CENPF$^+$ tumor cells resided at the terminal point of the differentiation trajectory, suggesting a decreased differentiation ability and a relatively restricted degree of diversification (Figures S4A–S4C). In summary, we identified two tumor cell subtypes with active proliferation in ESCC: C2 EZH2$^+$ tumor cells and C3 CENPF$^+$ tumor cells. However, it is worth mentioning that although these cells divide vigorously, they dominate at the end of the differentiation trajectory.

T cell-mediated microenvironment immunosuppression in ESCC

As a pivotal cellular component within the immune microenvironment, T cells predominantly originated from LN samples (Figures 1F and S5A). Upon examination of Figure S5A, it is evident that CD4$^+$ T cells can be further classified into nine discrete subtypes, encompassing three types of naive T cells, two types of actively proliferating T cells, one effector T cell type, one regulatory T (Treg) cell type, and two types of follicular helper T (Tfh) cells. Proliferating CD4$^+$ T cells and CD4 TIGIT$^+$ Treg cells were primarily derived from tumor tissues, indicating that tumor tissues may possess a more active immunosuppressive microenvironment than metastatic tissues (Figures S5B and S5C). Among these, CD4 TOP2A$^+$ proliferating Treg cells exhibited the most elevated G2M value, whereas CD4 STMN1$^+$ proliferating Treg cells displayed the highest S value (Figure S5F). Figures S5D and S5E showed key marker genes associated with distinct CD4$^+$ T cell subtypes. We further explored the biological functional heterogeneity of CD4$^+$ T cell subtypes (Figures S6A–S6E).

The CD8$^+$ T cell population comprised three subtypes of naive T cells, two subtypes of effector T cells, and three subtypes of depleted T cells (Figures S7A–S7C). Bubble and uniform manifold approximation and projection (UMAP) plots were used to visualize the distribution patterns of marker genes across these distinct subtypes (Figures S7D and S7E).

CellPress
OPEN ACCESS

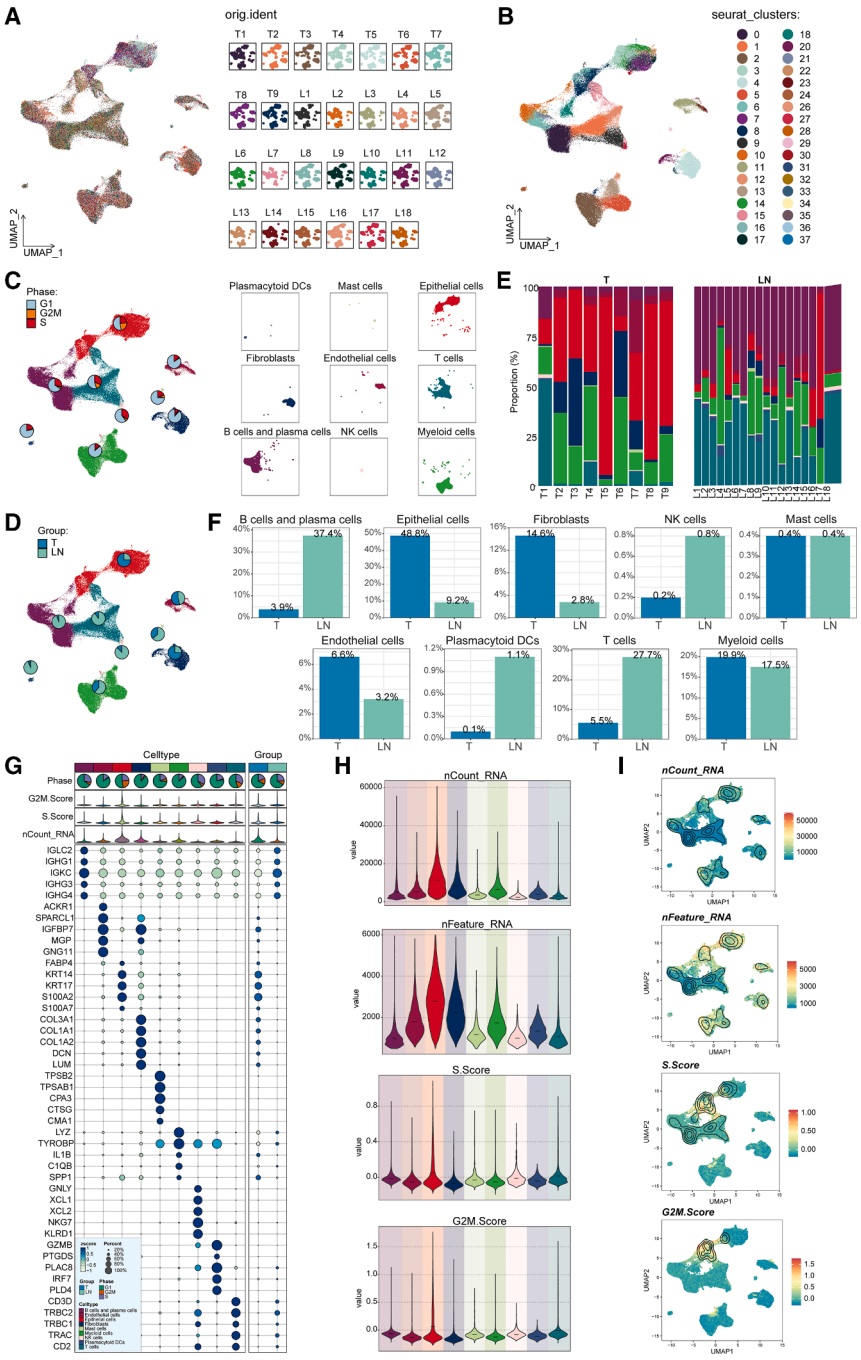

Figure 1. Identification of ESCC cell types based on specific markers among 9 clusters

(A) Two-dimensional (2D) plots of UMAP dimensionality reduction of samples from different sources in single-cell transcriptome data for 121,038 high-quality cells.

(B) Cluster analysis was performed using the Seurat package to label the different cell types.

(C and D) UMAP plots showed 9 ESCC cell types upon re-clustering. The pie charts showed the distribution of 9 cell types in different phases (C) and different groups (D).

(E and F) The bar graphs showed the proportion of each cell type in the tumor (T) and lymph node (LN) groups.

(G) Expression of top 5 marker genes for each cell type and their expression in different groups (T and LN) and different phases (G1, S, and G2M).

(H) Violin plots showed the different values of different cell types in nFeature-RNA, nCount-RNA, G2M value, and S value.

(I) 2D plots of UMAP dimensionality reduction of nFeature-RNA, nCount-RNA, G2M value, and S value.

Notably, the cell cycle scores indicated vigorous proliferation of CD8 ANXA2$^+$ exhausted T cells (Figure S7F), potentially linked to their involvement in cellular metabolism (Figures S8A–S8E).

In summary, we performed a comprehensive and detailed characterization of CD4$^+$ T cells and CD8$^+$ T cells in ESCC and visualized the great heterogeneity of CD4$^+$ T cell subtypes and CD8$^+$ T cell subtypes in gene expression, biological function, and development trajectory.

ESCC immune profiles suggest the presence of specific subtypes of TAMs

TAMs are the most abundant immune cells in the TME, and they can evolve a variety of malignant phenotypes to interfere with the development of ESCC and occupy a dominant position in the immune microenvironment of ESCC. Hence, our subsequent focus was on investigating the distinctive characteristics of TAMs in ESCC. The results of dimensionality reduction clustering demonstrated that TAMs were divided into seven distinct subtypes: C0 TREM2$^+$ macrophages, C1 FN1$^+$ macrophages, C2 CD14$^+$ macrophages, C3 LGALS2$^+$ macrophages, C4 TNFAIP3$^+$ macrophages, C5 CHCHD6$^+$ macrophages, and C6 VCAM1$^+$ macrophages (Figure 2A). TAM subtypes show obvious distribution heterogeneity in ESCC samples. C0 TREM2$^+$ macrophages originated predominantly from LN samples in G1 and S phases. C1 FN1$^+$ macrophages were predominantly observed in tumor tissues undergoing active proliferation, primarily in the G2M and S phases. This suggests that a subtype of TAMs with vigorous division was found in the microenvironment of the primary tumor, which may be closely related to the tumor immune imbalance. In addition, C2 CD14$^+$ macrophages and C4 TNFAIP3$^+$ macrophages primarily originated from tumor tissues. On the other hand, C3 LGALS2$^+$ macrophages and C6 VCAM1$^+$ macrophages were predominantly derived from

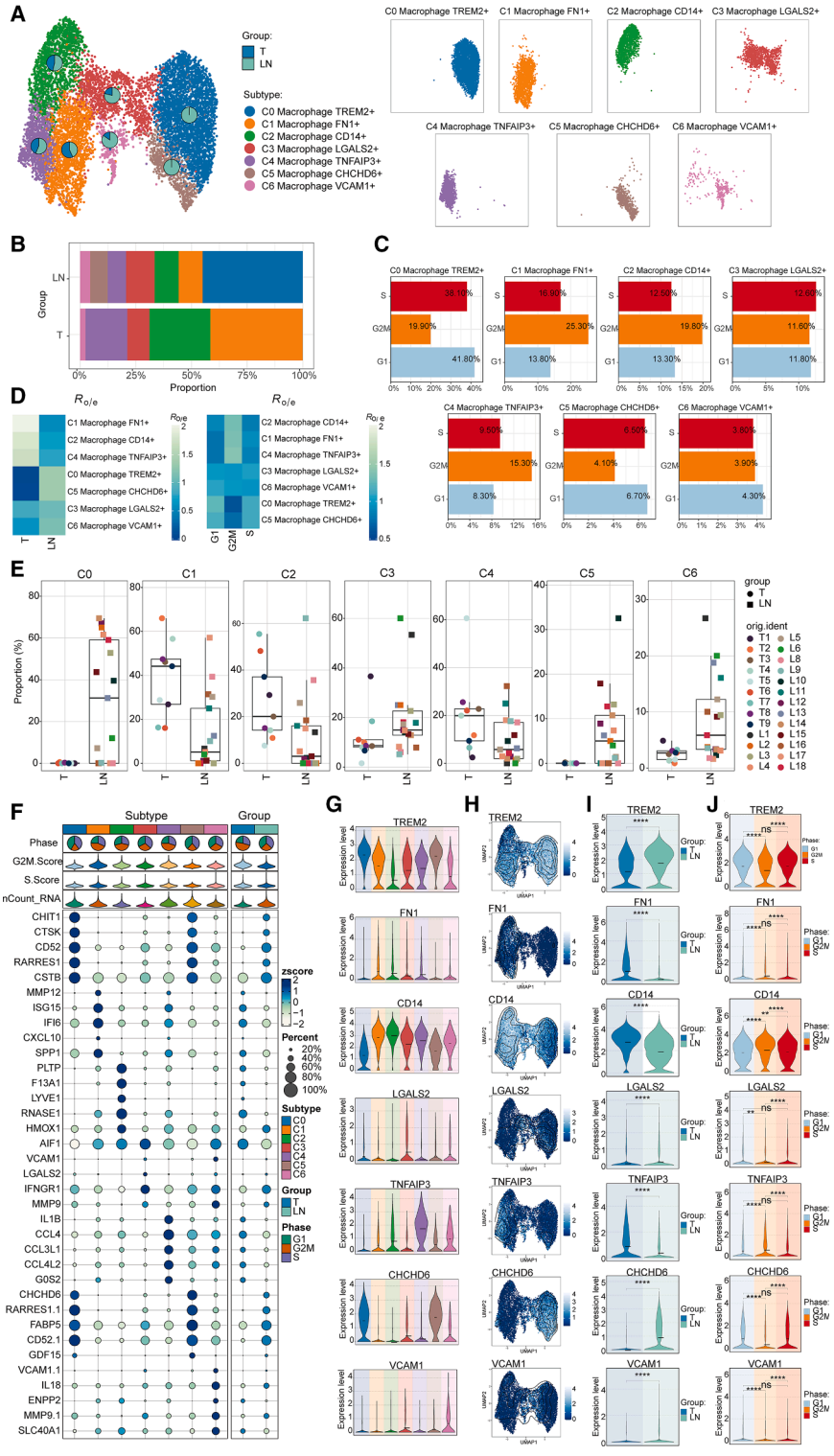

Figure 2. Seven subtypes of macrophages were identified using different markers

(A) The 2D plots of UMAP dimensionality reduction of the 10,102 macrophages.

(B and C) The percentages of groups and phases among cell types were represented on the proportion charts.

(D) Group and phase preference of each macrophage cluster estimated by Ro/e score.

(E) Plots compare the proportions of the 7 macrophage subtypes originating from different samples in different groups. An unpaired two-sided Wilcoxon test was used.

(F) Expression of top 5 marker genes in various macrophage subtypes and their expression in different groups, different phases, G2M values, S values, and nCount-RNAs.

(G and H) Violin and UMAP plots showed the expression of TREM2, FN1, CD14, LGALS2, TNFAIP3, CHCHD6, and VCAM1 in different macrophage subtypes.

(I) Differential expression levels of TREM2, FN1, CD14, LGALS2, TNFAIP3, CHCHD6, and VCAM1 between T and LN groups. An unpaired two-sided Wilcoxon test was used. $*p < 0.05$, $**p < 0.01$, $***p < 0.001$, $****p < 0.0001$, and ns indicates no statistical difference.

(J) Differential expression levels of TREM2, FN1, CD14, LGALS2, TNFAIP3, CHCHD6, and VCAM1 across G1, G2M, and S phases. An unpaired two-sided Wilcoxon test was used. $*p < 0.05$, $**p < 0.01$, $***p < 0.001$, $****p < 0.0001$, and ns indicates no statistical difference.

metastasis-associated LNs (Figures 2B–2E). Different TAM subtypes had different characteristic gene expression patterns (Figure 2F). We showed the expression patterns of marker genes of different TAM subtypes in all directions using violin plots and UMAP plots (Figures 2G–2J). The expression of these marker genes was consistent with the distribution of their corresponding TAM subtypes in sample grouping and cell phases.

Enrichment analysis reveals the biological functions of different subtypes of TAMs

The heterogeneity of the differential genes can provide enhanced insights into the biological attributes of various TAM subtypes (Figure S9A). Gene set enrichment analysis (GSEA) (Figure S9B) revealed a close association between C0 TREM2$^+$ macrophages and energy metabolism. These macrophages exhibited significant enrichment in pathways such as "cellular lipid metabolic process," "small molecule metabolic process," " aerobic respiration," and "electron transport chain." C1 FN1$^+$ macrophages, C2 CD14$^+$ macrophages, and C4 TNFAIP3$^+$ macrophages exhibit shared biological effects and demonstrate enrichment in immune-related pathways such as "defense response," "immune response," "response to cytokine," and

CellPress
OPEN ACCESS

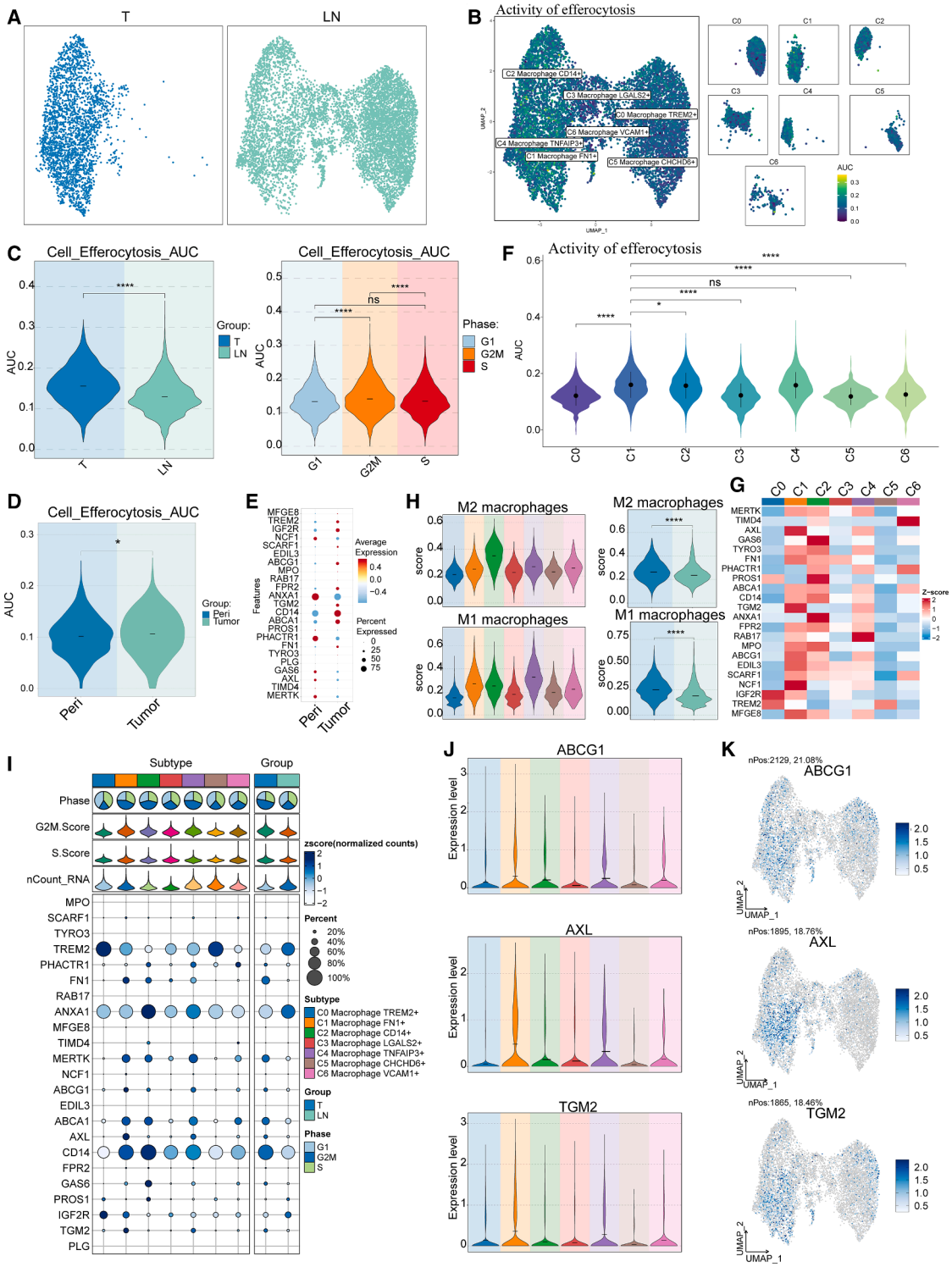

Figure 3. The role of macrophages in the activity of efferocytosis

(A) The UMAP plots showed macrophages from the T and LN groups, respectively.

(B) AUC values for efferocytosis activity in different macrophage subtypes. Colors that tend to be yellow indicate higher AUC values, and colors that tend to be bluer indicate lower AUC values.

(C) Comparison of AUC values for cell efferocytosis in different groups and phases. The Wilcoxon test was used for comparison between two groups, and the Kruskal test was used for comparison between multiple groups. *$p < 0.05$, **$p < 0.01$, ***$p < 0.001$, ****$p < 0.0001$, and ns indicates no statistical difference.

(legend continued on next page)

"cellular response to cytokine stimulus" (Figures S9B and S9D). Consonant with the GSEA findings, in GO-BP, C1 FN1$^+$ macrophages, C2 CD14$^+$ macrophages, and C4 TNFAIP3$^+$ macrophages had higher "leukocyte" and "immune" scores (Figure S9C). It can be concluded that there are several TAM subtypes with immune effects in ESCC; however, the functions of these subtypes in tumor immunity remain unclear.

Heterogeneity of efferocytosis activity in subtypes of TAMs

Immune function in tumors is closely linked to the efferocytosis activity of TAMs. Impaired efferocytosis reduces TAM recognition and engulfment of tumor cells, compromising immune surveillance and contributing to resistance to antitumor therapies.[15] To explore this, we assessed the efferocytosis potential of different TAM subtypes to identify immune-specific populations. TAMs within primary tumor tissues exhibited significantly higher efferocytosis activity compared to those from LNs (Figures 3A–3C). This suggests a stronger immunosuppressive environment at the primary tumor site, potentially making macrophage efferocytosis a promising therapeutic target for ESCC. *In vitro*, human primary macrophages were co-cultured with apoptotic ESCC cells (EC9706 and KYSE180) to evaluate their efferocytosis activity. Confocal microscopy and flow cytometry confirmed that treatment with bavituximab, a PS-targeting monoclonal antibody, reduced efferocytosis, as evidenced by decreased CMFDA$^+$ (CellTracker Green CMFDA, 492/517 nm) cells (Figure S10). Further analysis of scRNA-seq data revealed that efferocytosis activity was notably higher in tumor tissues than in normal tissues (Figures 3D and 3E). Among TAM subtypes, C1 FN1$^+$ macrophages showed the highest efferocytosis activity (Figures 3F and 3G), indicating a link between heightened efferocytosis and an immunosuppressive TME. C1 FN1$^+$ macrophages appeared to be in a transitional state between M1 and M2 phenotypes, influencing their immune function (Figure 3H). Genes associated with efferocytosis in the C1 FN1$^+$ subtype, including ABCG1, AXL, and TGM2, were found to regulate apoptosis and lipid metabolism, supporting the notion that TAM efferocytosis may be linked to lipid processing (Figures 3I–3K). This aligns with previous research suggesting a role for lipid metabolism in TAM-mediated efferocytosis.[16]

Differentiation potential and differentiation trajectories of TAMs

Trajectory analysis can reshape the change process of cells over time by constructing the change trajectory between cells to infer the evolution and differentiation process of different subtypes of TAMs at the single-cell level. First, we employed CytoTRACE to evaluate the stemness attributes of TAMs to determine their level of differentiation (Figures 4A and 4B). As illustrated in Figure 4C, the C1 FN1$^+$ macrophage population demonstrated the highest cellular stemness, indicating the lowest degree of differentiation, attenuated functionality, and heightened potential for differentiation. This may be related to the immune-related genes FCGR3A, C1QC, GAPDH, and TGFBI, which were positively correlated with cell stemness in CytoTRACE (Figure 4D). Figures 4E–4G show the expression of stemness genes in each TAM subtype.

Consistent with the CytoTRACE analysis, Slingshot results showed that TAM differentiation trajectories started at C1 FN1$^+$ macrophages in different tissue sources and cell cycles (Figures S11A and S11B). Similarly, C1 FN1$^+$ macrophages were at an early stage of cellular differentiation in two differentiation trajectories of TAM subtypes (Figures S11C and S11E). Enrichment analysis (Figures S11D and S11F) revealed that in the first differentiation track, the C1 FN1$^+$ macrophage subtype exhibited enrichment in pathways associated with "peptidase," "endopeptidase," and "activity." These proteases have been shown to affect the efferocytosis effect of TAMs.[17] On the other hand, in the second differentiation trajectory, the C1 FN1$^+$ macrophage subtype displayed predominant enrichment in immune-related pathways, including "leukocyte," "immune," and "lymphocyte" pathways. From the point of view of cell development and differentiation, CytoTRACE and Slingshot analyses showed that C1 FN1$^+$ macrophages had low differentiation and a high degree of malignancy, which may be related to the rapid progression of ESCC and poor prognosis.

To summarize, the above data indicate the identification of a distinctive subtype of TAMs within tumors. This subtype demonstrates pronounced proliferative characteristics, robust immunosuppressive functions, heightened efferocytosis activity, and a significant differentiation potential. These TAMs play a crucial role in the TME and contribute to immune resistance.

The transcription factor TP63 regulates the carcinogenic mechanism of C1 FN1$^+$ macrophages

Transcription factors regulate gene expression by binding to specific DNA sequences, controlling cellular functions and characteristics. In this study, we investigated the regulatory network of C1 FN1$^+$ macrophages using SCENIC analysis. Dimensionality reduction and cluster analysis of TAM subtypes based on gene expression and regulon activity revealed distinct subgroups, with significant differences in regulon activity among TAM subtypes but no variation between different cell phases (Figures S12A–S12C). This suggests that regulon activity plays a crucial role in TAM subtype classification. Further correlation analysis showed a strong association between TAM subtypes

(D) Comparison of AUC values of macrophage efferocytosis activity in ESCC tumor samples and normal samples from the GEO database. An unpaired two-sided Wilcoxon test was used. *$p < 0.05$, **$p < 0.01$, ***$p < 0.001$, ****$p < 0.0001$, and ns indicates no statistical difference.
(E) Differential expression of macrophage efferocytosis-related genes in ESCC tumor samples and normal samples from the GEO database.
(F and G) AUC values of efferocytosis activity and efferocytosis-related gene expression in the different macrophage subtypes. An unpaired two-sided Wilcoxon test was used. *$p < 0.05$, **$p < 0.01$, ***$p < 0.001$, ****$p < 0.0001$, and ns indicates no statistical difference.
(H) Score of M1- and M2-related genes in different macrophage subtypes and groups. An unpaired two-sided *t* test was used. *$p < 0.05$, **$p < 0.01$, ***$p < 0.001$, ****$p < 0.0001$, and ns indicates no statistical difference.
(I) Expression of efferocytosis genes in each macrophage subtype and different groups, different phases, G2M values, S values, and nCount-RNA.
(J and K) Expression levels and distribution of three representative efferocytosis genes, TGM2, AXL, and ABCG1, in different macrophage subtypes.

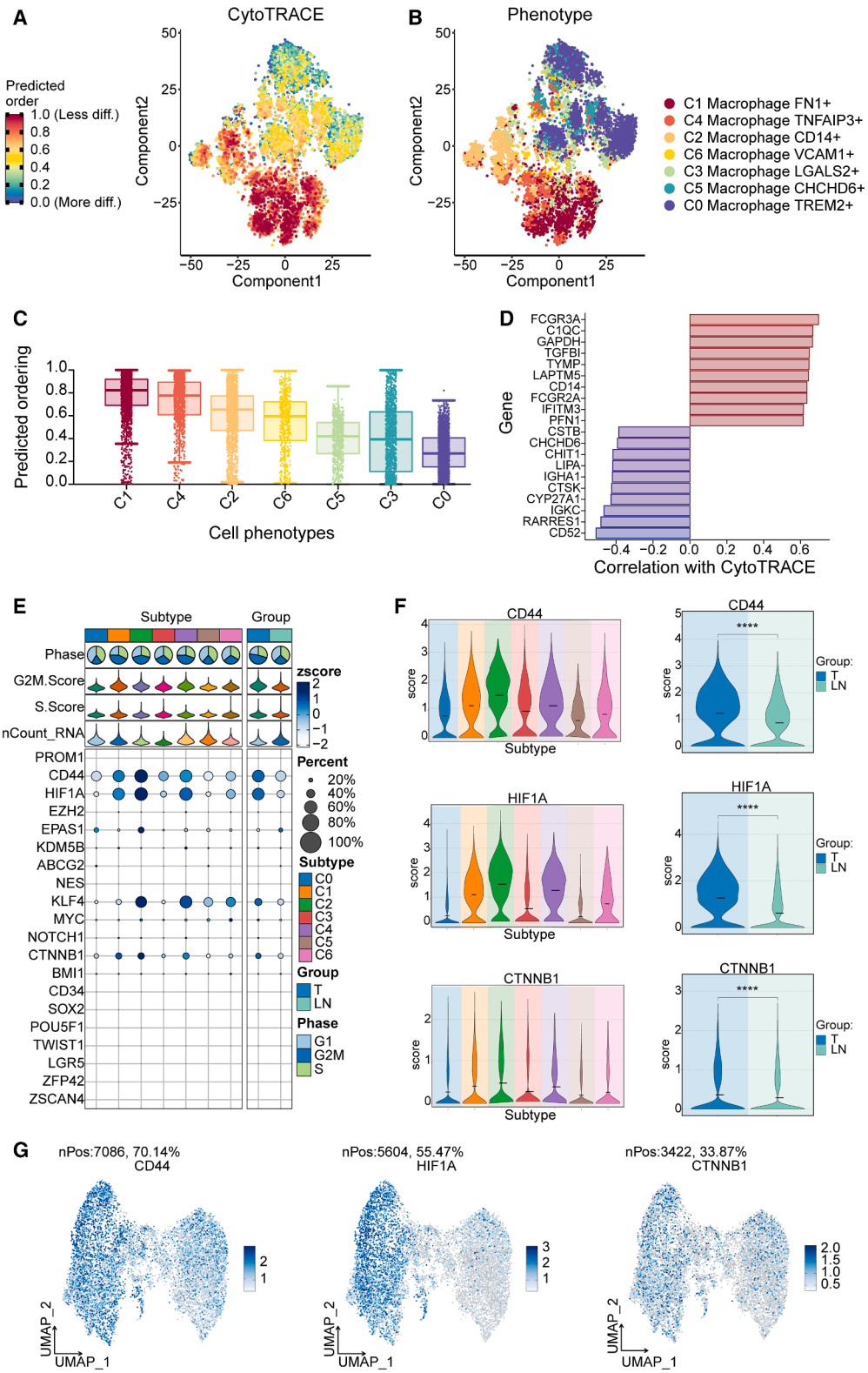

Figure 4. Visualization of macrophage differentiation trajectories and differentially expressed stemness genes

(A) Differentiation trajectories obtained using CytoTRACE.

(B) Distribution of 7 macrophage subtypes.

(legend continued on next page)

from different sample groups, including C2 CD14$^+$ macrophages, C1 FN1$^+$ macrophages, C3 LGALS2$^+$ macrophages, and C4 TNFAIP3$^+$ macrophages (Figure S12D). We identified key regulatory submodules for TAM subtypes M1, M2, M3, and M4 using the connection specificity index (CSI), highlighting the collaboration of transcription factors in gene regulation (Figure S12E). Notably, the M1 submodule was the primary regulator for C1 FN1$^+$ macrophage and other TAM subtypes, as well as their grouping (Figures S12F–S12H). Among the top five key regulators for C1 FN1$^+$ macrophages (KLF5, ETV6, TP63, RUNX3, and ETV7), TP63 and KLF5 showed the highest significance in distinguishing TAM subtypes and groups (Figures 5A and S12I). Further analysis confirmed that the area under the curve (AUC) for TP63 and KLF5 was more prominent in these subtypes (Figures 5B and S12J). These findings suggest that TP63 and KLF5 play critical roles in regulating the carcinogenic mechanisms of C1 FN1$^+$ macrophages, with TP63, in particular, emerging as a key driver in the regulation of TAM biological functions.

Knockdown of TP63 impairs the *in vitro* efferocytosis of macrophages

We analyzed the effects of TP63 and KLF5 on macrophage efferocytosis using gene knockdown. Macrophages were transfected with siTP63 or siKLF5, and siTP63-3 or siKLF5-3 induced the most significant reduction of TP63 or KLF5 in human primary macrophages (Figure 5C), THP-1, mouse primary macrophages, and RAW264.7 cells (Figure S13) and was selected for the following experiments. To determine *in vitro* efferocytosis, human primary macrophages were co-cultured with apoptotic esophageal carcinoma cells (EC9706 and HYSE180), and ingestion of these fluorescent cells was assessed by confocal imaging and flow cytometry. As depicted in Figures 5D–5G, human primary macrophages engulfed CMFDA-labeled EC9706 and HYSE180, whereas the ability of TP63-depleted macrophages to take up ACs was notably reduced. These data indicate that the knockdown of TP63 repressed the efferocytosis ability of macrophages.

TP63 modulates RAC2 expression in macrophages

To understand how TP63 regulates the efferocytosis of macrophages, we analyzed differentially expressed genes (DEGs) between wild-type and TP63-depleted human primary macrophages after co-culture with apoptotic EC9706 cells (Figure S14A). The DEGs were mainly enriched in terms correlated with mitochondrial structure and function, ribosome subunit, cell cycle, and thermogenesis (Figures S14B and 14C). We further verified the alteration of representative genes in TP63-depleted macrophages, among which the RAC2 level was the most obviously changed (Figures S14D and 14E). In addition, we confirmed the downregulation of RAC2 mRNA and protein levels by siTP63 in multiple macrophages, including human primary macrophages, bone-marrow-derived macrophages (BMDMs), THP-1 cells, and RAW264.7 cells, respectively (Figures S14F and S14G). To investigate whether TP63 functions as a transcriptional factor for RAC2, we predicted the potential binding site of TP63 in the upstream promoter region (−1,405 to +20 bp) of RAC2 (Figure S14H). Subsequently, we constructed luciferase reporter gene vectors containing truncated promoter fragments based on the predicted binding sites and analyzed luciferase activity. As shown in Figure S14I, compared with the full-length constructs (P6), the constructs containing both binding site 1 and binding sites 2/3 (P5, P4, and P3) and the construct containing only binding site 2/3 (P2) exhibited no obvious change in luciferase activity, whereas the deletion of binding site 2/3 (P1) significantly reduced luciferase activity. These results indicate that TP63 potentially interacts with the RAC2 promoter at binding sites 2/3. Furthermore, we observed that the knockdown of TP63 markedly downregulated the luciferase activity of P6 and P2 in human primary macrophages (Figures S14J and S14K) and THP-1 cells (Figures S14L and S14M). The results from the chromatin immunoprecipitation (ChIP) experiment showed that TP63 directly binds to the RAC2 gene, which is notably repressed by siTP63 (Figures S14N and S14O). In clinical samples, we observed that the efferocytosis of TP63+ and RAC2+ macrophages was enhanced in positive LN samples compared to negative LN samples by multiplex immunohistochemistry (mIHC) assay and image analysis (Figure S15). These data suggested that TP63 interacts with RAC2 to promote its transfection and expression.

TP63-mediated *in vitro* efferocytosis contributes to the polarization of macrophages via RAC2

Subsequently, we validated the effects of RAC2 as a downstream regulator of TP63 expression. Primary macrophages were depleted of TP63 and rescued by RAC2 overexpression, and *in vitro* efferocytosis and polarization of macrophages were analyzed. As shown in Figure 6A, overexpression of RAC2 resulted in the recovery of RAC2 expression in TP63-deleted macrophages. Macrophages were then incubated with CMFDA-labeled apoptotic EC9706 cells, and RAC2 overexpression in macrophages significantly recovered the TP63-suppressed engulfment of ACs (Figures 6B–6E). To determine whether TP63/RAC2-mediated efferocytosis is a critical driving force for M2 macrophage polarization, primary macrophages were co-cultured with CMFDA-labeled apoptotic EC9706 cells to analyze the macrophage phenotype. Flow cytometry analysis showed that TP63 knockdown significantly reduced the population of M2 macrophages (F4/80$^+$CD163$^+$

(C) Ranking of macrophage differentiation according to CytoTRACE. The lowest differentiation of C1 FN1$^+$ macrophages and the highest differentiation of C0 TREM2$^+$ macrophages could be observed in the graph.
(D) Major regulatory genes that regulated macrophage differentiation.
(E) Visualization of stemness gene expression characteristics in different macrophage subtypes and different groups (T and LN), different phases (G1, S, and G2M), G2M values, S values, and nCount-RNAs.
(F) Differential score of representative marker genes CD44, HIF1A, and CTNNB1 in the T and LN groups and different subtypes. An unpaired two-sided Wilcoxon test was used. *$p < 0.05$, **$p < 0.01$, ***$p < 0.001$, ****$p < 0.0001$, and ns indicates no statistical difference.
(G) The UMAP plots showed the expression of CD44, HIF1A, and CTNNB1 in the macrophages.

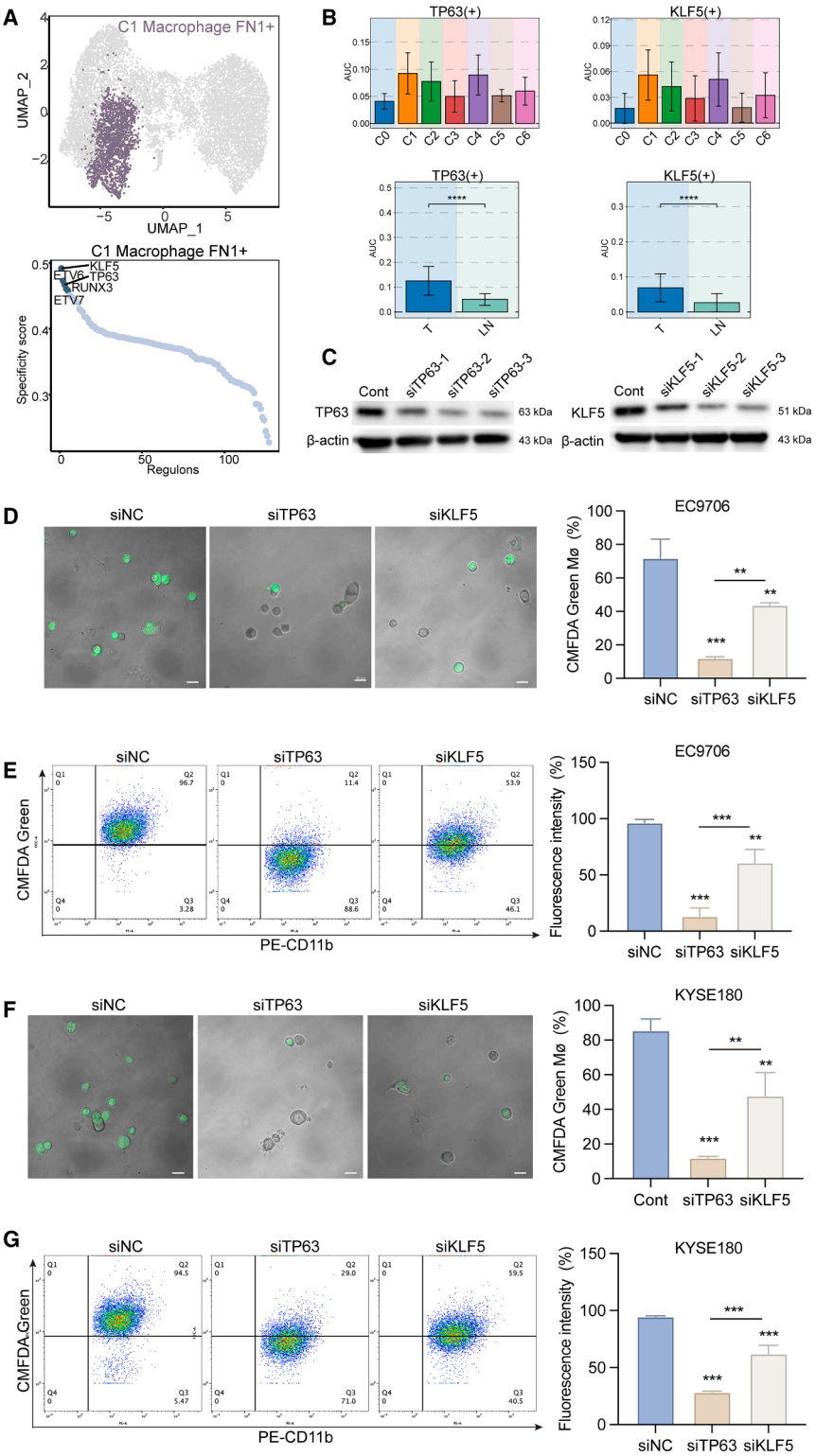

Figure 5. Identification of regulator TP63 and verification of its biological function *in vitro*

(A) C1 FN1$^+$ macrophage is highlighted in the UMAP plot (dark purple) (top); rank for regulons in C1 FN1$^+$ macrophages is based on regulon specificity score (RSS, below).

(B) The AUC of key regulators TP63 and KLF5 in C1 FN1$^+$ macrophages in different TAM subtypes (top) and different groups (below). An unpaired two-sided Wilcoxon test was used. $^*p < 0.05$, $^{**}p < 0.01$, $^{***}p < 0.001$, $^{****}p < 0.0001$, and ns indicates no statistical difference.

(C) Human primary macrophages were transfected with siTP63 or siKLF5, and TP63 or KLF5 protein expression was detected by western blotting.

(D and E) The apoptotic EC9706 cells (ACs) were labeled with CMFDA and incubated with wild-type or TP63-depleted human primary macrophages. The efferocytosis of apoptotic EC9706 by macrophages was examined by (D) confocal imaging and (E) flow cytometry. The white scale bar represents 20 μm.

(F and G) The apoptotic HYSE180 cells (ACs) were labeled with CMFDA and incubated with wild-type or TP63-depleted human primary macrophages. The efferocytosis of ACs by macrophages was examined by (F) confocal imaging (green dots) and (G) flow cytometry (CMFDA$^+$PE-CD11b$^+$ cells). $^{***}p < 0.001$. The white scale bar represents 20 μm. Data are presented as the mean ± SD of five independent experiments.

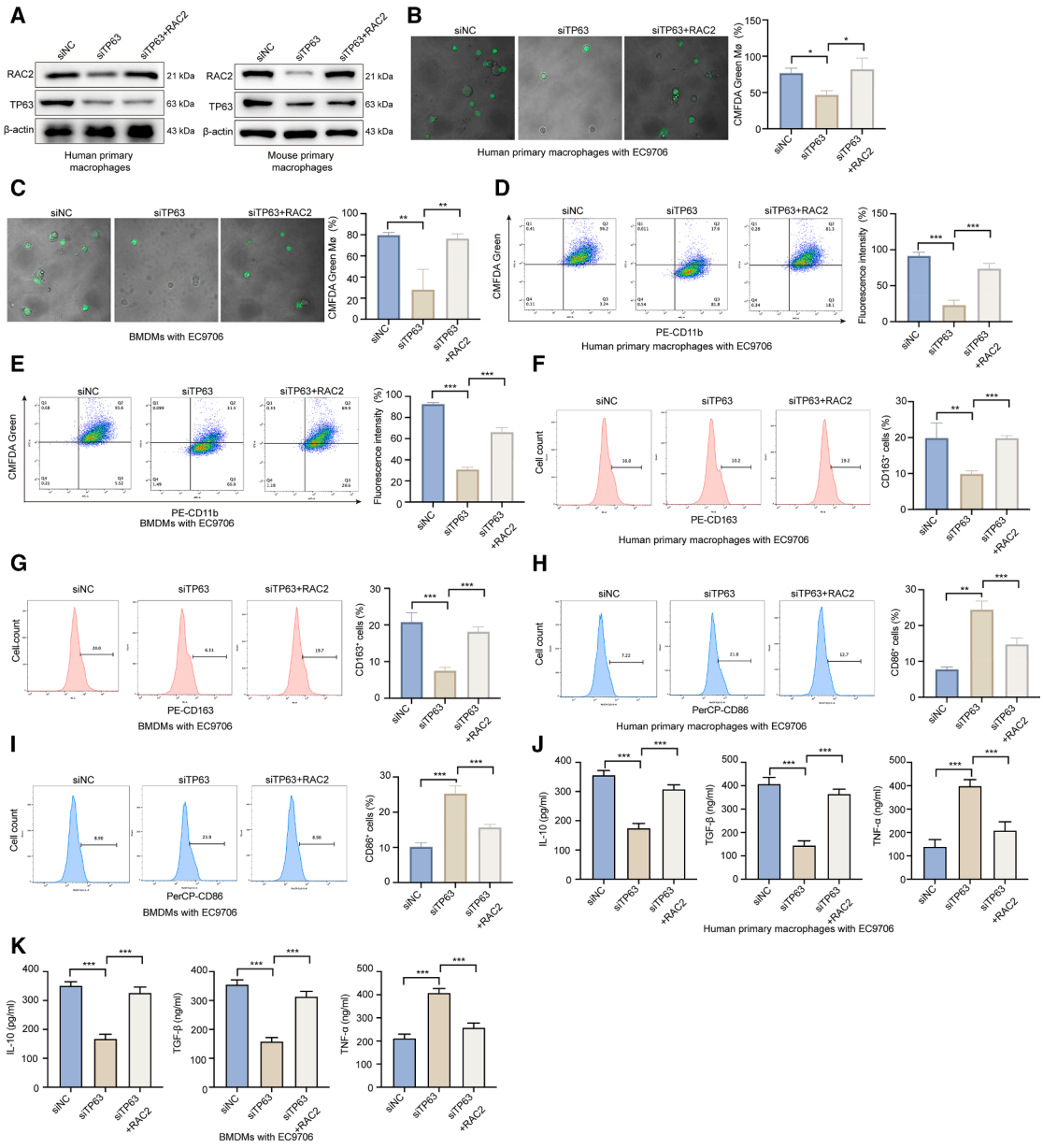

Figure 6. Efferocytosis and polarization of macrophages were analyzed *in vitro*

(A) Western blotting verifies the differences in TP63 and RAC2 protein expression levels in the shTP63 and shTP63+RAC2 groups compared with the control group.

(B) Differences in the fluorescence signal intensity of CMFDA green among groups of human primary macrophages with EC9706. *$p < 0.05$.

(C) Differences in the fluorescence signal intensity of CMFDA green among groups in THP-1-induced macrophages with EC9706. **$p < 0.01$.

(D) The fluorescence signal intensity of CMFDA green in human primary macrophages treated with EC9706 was determined by flow cytometry. ***$p < 0.001$.

(E) The fluorescence signal intensity of CMFDA green in THP-1-induced macrophages treated with EC9706 was determined by flow cytometry. ***$p < 0.001$.

(F) The $CD163^+$ cell level of each group in human primary macrophages with EC9706. **$p < 0.01$, ***$p < 0.001$.

(G) The $CD163^+$ cell level of each group in THP-1-induced macrophages with EC9706. ***$p < 0.001$.

(H) The $CD86^+$ cells in each group of human primary macrophages treated with EC9706. **$p < 0.01$, ***$p < 0.001$.

(I) The $CD86^+$ cells in each group of THP-1-induced macrophages treated with EC9706. ***$p < 0.001$.

(J) Differences in IL-10, TGF-β, and TNF-α levels among the groups in human primary macrophages with EC9706. ***$p < 0.001$.

(K) Differences in IL-10, TGF-β, and TNF-α levels among the groups in THP-1-induced macrophages with EC9706. Data are presented as the mean ± SD of five independent experiments. ***$p < 0.001$.

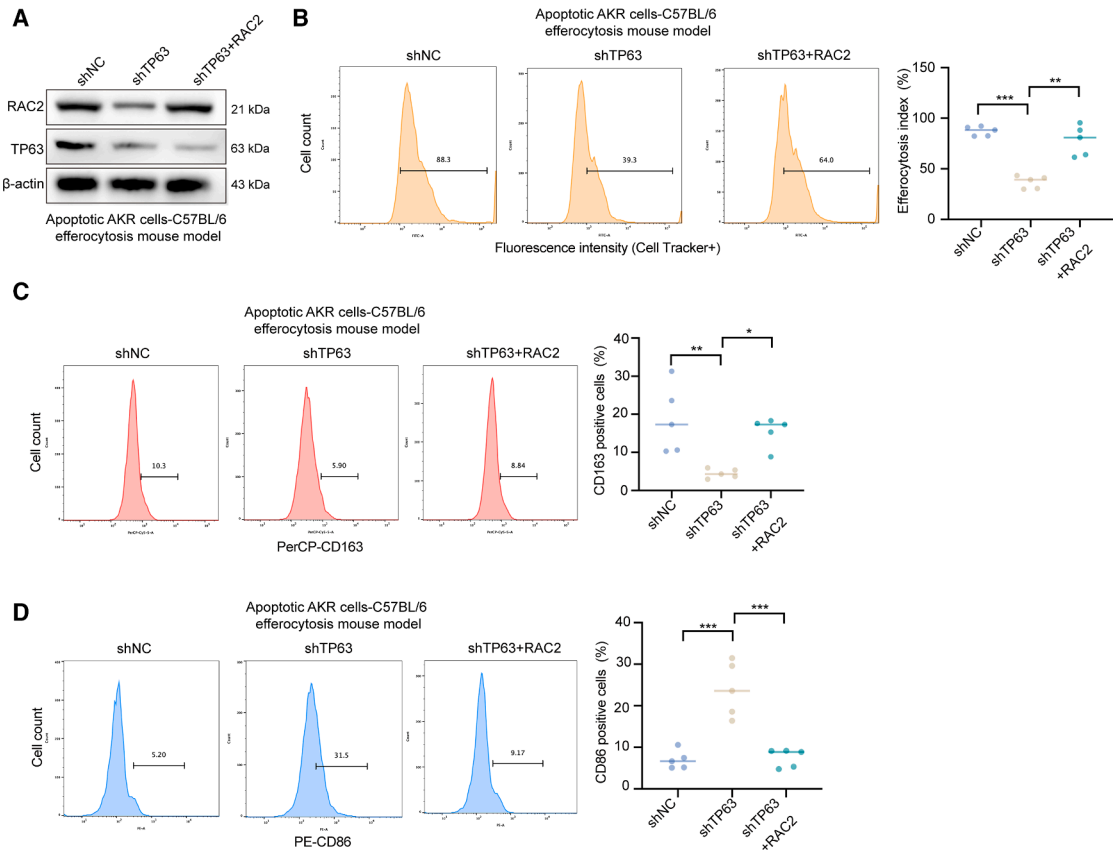

Figure 7. Experimental study of shTP63 and shTP63+RAC2 in apoptotic AKR (apoptotic esophageal carcinoma) cells-C57BL/6 efferocytosis mouse model

(A) Western blot verifies the difference in TP63 and RAC2 protein expression levels in shTP63 and shTP63+RAC2 groups compared with the control group.

(B) The efferocytosis index level of each group was detected ($n = 5$ per group). $^{**}p < 0.01$, $^{***}p < 0.001$.

(C) The CD163^{+} cells in each group were detected ($n = 5$ per group). $^{*}p < 0.05$, $^{**}p < 0.01$.

(D) The CD86^{+} cells in each group ($n = 5$ per group). $^{**}p < 0.01$, $^{***}p < 0.001$.

cells) (Figures 6F and 6G) and increased the population of M1 macrophages (F4/80^{+}CD86^{+} cells) (Figures 6H and 6I) following co-culture with ACs, whereas overexpression of RAC2 reversed these phenotypic changes. To further elucidate the effects of TP63/RAC2-mediated efferocytosis on macrophage polarization, the expression of M2- and M1-type genes was assayed. The TP63-depleted macrophages exhibited downregulated production of interleukin (IL)-10 and transforming growth factor β (TGF-β) (M2-type biomarker) and upregulated the level of tumor necrosis factor alpha (TNF-α) (M1-type biomarker) compared with the control cells, which was reversed by RAC2 overexpression (Figures 6J and 6K). These data indicate that TP63-dependent efferocytosis *in vitro* modulates M2 polarization of macrophages by regulating RAC2.

TP63/RAC2 signaling regulates the *in vivo* efferocytosis

We investigated the role of TP63/RAC2 signaling in *in vivo* efferocytosis using a peritoneal injection of ACs and a thymus efferocytosis assay. Mice were pretreated with shTP63 and RAC2 overexpression vectors, followed by peritoneal injection of apoptotic esophageal carcinoma cells (AKR). Peritoneal macrophages were then isolated for efferocytosis and polarization analysis. Treatment with shTP63 reduced RAC2 expression, while RAC2 overexpression restored it (Figure 7A). *In vivo* efferocytosis of fluorescent ACs by peritoneal macrophages was impaired following shTP63 treatment, but RAC2 overexpression recovered efferocytosis levels (Figure 7B). Additionally, shTP63-treated macrophages exhibited a decreased M2 phenotype and increased M1 polarization, which was reversed by RAC2 overexpression (Figures 7C and 7D). To further explore these effects, we induced thymocyte apoptosis with dexamethasone after treating mice with shTP63 and RAC2 vectors. Overexpression of RAC2 rescued RAC2 levels in macrophages (Figure S16A), and decreased efferocytosis of apoptotic thymocytes in the shTP63 group was reversed by RAC2 overexpression (Figure S16B). Thymic macrophages from shTP63-treated mice showed M1 polarization, and RAC2 overexpression restored M2 polarization (Figures S16C and S16D). These results confirm that TP63/RAC2 signaling regulates *in vivo* efferocytosis by macrophages. Next, we examined the impact of TP63/RAC2 on tumor progression

using EC9706 cells in a humanized mouse model. TP63 knockdown significantly suppressed tumor growth, highlighting its role in regulating tumor progression. However, RAC2 overexpression reversed these effects, suggesting RAC2's critical role in tumor growth regulation (Figures S17A–S17C). Further analysis showed that TP63 knockdown decreased efferocytosis *in vivo* (Figure S17D) and shifted macrophage polarization toward the M1 phenotype, which is pro-inflammatory and antitumor. RAC2 overexpression restored efferocytosis levels and M2 polarization (Figures S17D–S17F). Additionally, RAC2 knockdown impaired efferocytosis in both EC9706 and KYSE180 cells, as confirmed by confocal microscopy and flow cytometry (Figure S18), further supporting RAC2's role in regulating macrophage function and efferocytosis within the TME. These findings suggest that efferocytosis, modulated by the TP63-RAC2 axis, influences the proliferative and metastatic behavior of ESCC cells by shaping the TME. Targeting efferocytosis and its regulatory pathways, such as TP63/RAC2 signaling, holds therapeutic potential for ESCC treatment.

DISCUSSION

This study investigated the role of efferocytosis in ESCC by utilizing scRNA-seq and a variety of *in vitro* and *in vivo* experimental methods to reveal the heterogeneity of different cell types within the TME, particularly TAMs. Our findings provide compelling evidence that efferocytosis plays a pivotal role in the proliferative and metastatic behavior of ESCC cells, primarily through its effects on macrophage polarization and the TME. These insights underscore the therapeutic potential of targeting efferocytosis and its regulatory pathways, particularly the TP63-RAC2 axis, in the treatment of ESCC.

These findings offer therapeutic strategies for ESCC, suggesting that modulating the efferocytosis pathway can enhance antitumor immunity and improve patient outcomes.

Efferocytosis is a critical physiological process through which macrophages recognize and engulf ACs to maintain tissue homeostasis.[18–20] Within the TME, efferocytosis aids in clearing dead cells and modulates immune responses by secreting anti-inflammatory cytokines.[21] However, our research indicates that alterations in the efferocytosis process in ESCC may promote tumor growth and progression. The scRNA-seq results revealed that TAMs exhibit enhanced immunosuppressive characteristics after engulfing ACs, which may be a mechanism by which tumors evade immune surveillance.

We identified TP63 and RAC2 as crucial factors in efferocytosis regulation. TP63, a transcription factor, influences macrophage efferocytosis capacity by regulating the expression of RAC2. *In vitro* experiments demonstrated that TP63 knockdown significantly reduces macrophage efferocytosis, while RAC2 overexpression partially rescues this effect, restoring efferocytosis and macrophage polarization toward the M2 phenotype. Statistical analysis confirmed that RAC2 overexpression does not completely restore efferocytosis activity to control levels, suggesting that additional factors may contribute to the regulation of this pathway. These results suggested that TP63 and RAC2 are potential therapeutic targets. Modulation of these molecules can alter TAM functions, thereby enhancing antitumor immunity.

Efferocytosis involves not only the physical engulfment of cells[22] but also the regulation of the immune system.[23] After engulfing ACs, macrophages secrete a range of anti-inflammatory cytokines, such as IL-10 and TGF-β, to suppress immune responses.[24,25] This immunosuppressive environment helps tumor cells evade immune surveillance and promotes tumor growth.[26] Our study further suggests that intervention in the efferocytosis process can alter the immune status within the TME, thereby inhibiting tumor progression.

Current treatment strategies for ESCC primarily include surgery, radiotherapy, and chemotherapy.[27,28] However, these methods have limited efficacy, particularly in advanced-stage patients. Therefore, the development of therapeutic strategies is imperative.[29–31] Our study proposes an approach to enhance antitumor immunity by modulating efferocytosis. Specifically, targeting TP63 and RAC2 can alter TAM functions, reduce their immunosuppressive effects, and thereby enhance the ability of the immune system to attack tumors. This approach not only offers a therapeutic strategy but can also be combined with existing treatments to improve overall efficacy.

Although this study focuses on ESCC, efferocytosis plays a significant role in other cancer types as well.[32] For instance, in breast[33] and lung[34] cancers, efferocytosis is associated with tumor immune evasion and progression. Exploring the role of efferocytosis in various cancer types can provide targets and strategies for cancer treatment.[35] Additionally, comparing the mechanisms of efferocytosis across different cancer types can reveal its generality and specificity in tumor biology, thereby providing a basis for personalized therapy. Our study paves the way for several clinical translational applications. First, therapies targeting TP63 and RAC2 could be integrated with current treatment regimens to enhance their efficacy. For example, combining small-molecule inhibitors or antibodies against TP63 and RAC2 with immune checkpoint inhibitors could synergistically enhance antitumor immunity. Second, the identification of efferocytosis-related biomarkers could enable personalized treatment by stratifying patients based on their likelihood of responding to efferocytosis-targeted therapies. Finally, these strategies could extend beyond ESCC to other cancers, broadening their clinical impact.

Future research will focus on the following aspects. To increase the reliability and generalizability of our findings, we plan to validate them in a larger cohort of patients with ESCC. We will also consider the clinical characteristics of different patients, such as age, gender, and tumor stage, to explore how these factors influence efferocytosis and TAM function and address issues such as potential gender bias in our study. Although our study preliminarily revealed the roles of TP63 and RAC2 in efferocytosis, the specific molecular mechanisms remain unclear. We will use gene-editing technologies such as CRISPR-Cas9 to further investigate the functions and interactions of these two genes in macrophages. Additionally, through proteomic and transcriptomic analyses, we aimed to identify additional downstream effectors related to TP63 and RAC2. In addition, based on our findings, we will explore the development of antitumor therapies that modulate TP63 and RAC2. Specifically, we designed and screened small-molecule inhibitors or antibodies targeting these two molecules and

tested their antitumor efficacy in mouse models. We will also study the combination of these therapeutic strategies with existing treatments (such as immune checkpoint inhibitors) to achieve better therapeutic outcomes. To translate our basic research findings into clinical applications, we plan to collaborate closely with clinicians to design and conduct clinical trials to verify the efficacy and safety of therapies that target the efferocytosis pathway. We will also explore the development of biomarkers to identify patients who are likely to benefit from these therapies, thereby enabling personalized treatment.

In conclusion, we revealed the pivotal role of efferocytosis in ESCC progression. Through scRNA-seq and functional assays, we demonstrated that macrophage-mediated efferocytosis, regulated by TP63 and RAC2, significantly influences the TME. Disruption of these pathways alters macrophage efferocytosis, immune modulation, and tumor dynamics, suggesting potential therapeutic targets. Our findings show that TP63/RAC2 signaling regulates macrophage polarization, impacting tumor growth and immune suppression. *In vivo* experiments further confirmed these effects, supporting the therapeutic value of targeting efferocytosis pathways in ESCC. This research not only enhances our understanding of tumor-immune interactions but also paves the way for cancer therapies aimed at improving patient outcomes.

Limitations of the study

This study has several limitations that should be addressed in future research. The relatively small sample size (nine patients) may limit the generalizability of our findings, and larger cohorts are needed for validation. While scRNA-seq provided valuable insights into the TME, the exact mechanistic interactions between TP63, RAC2, and other immune regulators remain unclear and warrant further investigation through more targeted functional assays. Additionally, our focus on macrophage-mediated efferocytosis should be expanded to include other immune cells, such as T cells and fibroblasts, to better understand the full complexity of the immune landscape in ESCC. Finally, while TP63 and RAC2 are promising therapeutic targets, their potential clinical applications require deeper exploration of their precise molecular mechanisms, delivery strategies, and long-term effects on tumor immunity. These areas of research will be crucial for translating our findings into viable therapeutic strategies.

RESOURCE AVAILABILITY

Lead contact

Requests for further information, resources, and reagents should be directed to and will be fulfilled by the lead contact, Weiyu Shen (shenweiyu@nbu.edu.cn).

Materials availability

This study did not generate new reagents or materials.

Data and code availability

- The raw sequence data reported in this paper have been deposited in the Genome Sequence Archive in National Genomics Data Center, China National Center for Bioinformation/Beijing Institute of Genomics, Chinese Academy of Sciences (accession GSA number: HRA013708) and are publicly accessible at https://ngdc.cncb.ac.cn/gsa or https://ngdc.cncb.ac.cn/gsa-human/s/L5fjh7I1.
- No original code was generated for this study. All software and algorithms used in this study have been disclosed and cited in the STAR Methods section.
- Any additional information required to reanalyze the data reported in this paper is available from the lead contact upon request.

ACKNOWLEDGMENTS

This work was supported by the National Natural Science Foundation of China (82560462); Jiangxi Provincial Natural Science Foundation (20252BAC240428); the Ningbo Natural Science Foundation (2022J256); and the National Key R&D Program of China (no. 2022YFC3400803). J.C. acknowledges the national funds through FCT - Fundação Ciência e a Tecnologia, I.P., within the scope of UID/04923 and the FCT grant LISBOA2030-FEDER-00862500-14998.

AUTHOR CONTRIBUTIONS

Y.X. led the experimental design, scRNA-seq analysis, and functional assays. Z.Z. and Y.Z. conducted the data analysis and interpretation. C.Y., Y.L., and X.X. supported sample collection and provided technical assistance. W.J., C.L., and K.Z. provided input on the experimental design and *in vivo* assays. B.Y., J.C., S.L., S.H. and W.S. supervised the project and contributed to the manuscript preparation. All authors approved the final manuscript.

DECLARATION OF INTERESTS

J.C. is a co-founder and shareholder of TargTex S.A. - Targeted Therapeutics for Glioblastoma Multiforme. J.C. is a member of the Global Burden Disease (GBD) consortium of the Institute for Health Metrics and Evaluation (IHME), University of Washington (US), and is on the scientific advisory board of Vector Bioscience Cambridge.

STAR★METHODS

Detailed methods are provided in the online version of this paper and include the following:

- KEY RESOURCES TABLE
- EXPERIMENTAL MODEL AND STUDY PARTICIPANT DETAILS
  - Human specimens
  - Humanized PBMC mouse model
  - Cell culture
- METHOD DETAILS
  - Data of single cell cource collection
  - Single cell suspensions, library construction, and sequencing
  - Single-Cell RNA-Seq data processing
  - Determination of cell subtypes
  - Pathway enrichment analysis
  - Identification and analysis of malignant cells with copy number variation (CNV) estimation
  - Cell stemness and developmental trajectory inference
  - Transcription factor analysis
  - Laboratory animal culture
  - Preparation of macrophage differentiated cells
  - Isolation of primary macrophages
  - Cell transfection
  - *In vitro* efferocytosis assay
  - RNA sequencing
  - Total RNA extraction, cDNA synthesis, and quantitative PCR (qPCR)
  - Western blotting assay
  - Luciferase reporter gene assay
  - Chromatin immunoprecipitation (ChIP) assay
  - *In vivo* efferocytosis
  - *In vivo* thymus efferocytosis assay
  - Enzyme linked immunosorbent assay (ELISA)
  - Flow cytometry

- mIHC assay and image analysis
- QUANTIFICATION AND STATISTICAL ANALYSIS

SUPPLEMENTAL INFORMATION

Supplemental information can be found online at https://doi.org/10.1016/j.xcrm.2025.102529.

Received: August 2, 2024
Revised: January 2, 2025
Accepted: November 20, 2025
Published: December 18, 2025

REFERENCES

1. Ke, S., Fang, M., Li, R., Wang, J., and Lu, J. (2022). Downregulation of long noncoding RNA breast cancer anti-estrogen resistance 4 inhibits cell proliferation, invasion, and migration in esophageal squamous cell carcinoma by regulating the microRNA-181c-5p/LIM and SH3 protein 1 axis. Bioengineered *13*, 12998–13010.
2. Han, W., Wang, L., Li, C., Chen, J., Zhang, W., Wang, X., Pang, Q., Zhao, Y., Sun, X., Zhang, K., et al. (2022). Progression-free survival as surrogate endpoint of overall survival in esophageal squamous cell carcinoma: a real-world data and literature-based analysis. Ther. Adv. Med. Oncol. *14*, 17588359221131526.
3. Aasen, S.N., Parajuli, H., Hoang, T., Feng, Z., Stokke, K., Wang, J., Roy, K., Bjerkvig, R., Knappskog, S., and Thorsen, F. (2019). Effective Treatment of Metastatic Melanoma by Combining MAPK and PI3K Signaling Pathway Inhibitors. Int. J. Mol. Sci. *20*, 4235.
4. Wong, G.S., Lee, J.S., Park, Y.Y., Klein-Szanto, A.J., Waldron, T.J., Cukierman, E., Herlyn, M., Gimotty, P., Nakagawa, H., and Rustgi, A.K. (2013). Periostin cooperates with mutant p53 to mediate invasion through the induction of STAT1 signaling in the esophageal tumor microenvironment. Oncogenesis *2*, e59.
5. Zhang, J., Zhang, B., Pu, C., Cui, J., Huang, K., Wang, H., and Zhao, Y. (2023). Nanoliposomal Bcl-xL proteolysis-targeting chimera enhances anti-cancer effects on cervical and breast cancer without on-target toxicities. Adv. Compos. Hybrid Mater. *6*, 78.
6. Wu, S., Zhao, K., Wang, J., Liu, N., Nie, K., Qi, L., and Xia, L. (2022). Recent advances of tanshinone in regulating autophagy for medicinal research. Front. Pharmacol. *13*, 1059360.
7. Manoharan, M., Mandloi, N., Priyadarshini, S., Patil, A., Gupta, R., Iyer, L., Gupta, R., and Chaudhuri, A. (2018). A Computational Approach Identifies Immunogenic Features of Prognosis in Human Cancers. Front. Immunol. *9*, 3017.
8. Sun, Y., Zhang, Z., Zhang, C., Zhang, N., Wang, P., Chu, Y., Chard Dunmall, L.S., Lemoine, N.R., and Wang, Y. (2022). An effective therapeutic regime for treatment of glioma using oncolytic vaccinia virus expressing IL-21 in combination with immune checkpoint inhibition. Mol. Ther. Oncolytics *26*, 105–119.
9. Ambade, A., Satishchandran, A., Gyongyosi, B., Lowe, P., and Szabo, G. (2016). Adult mouse model of early hepatocellular carcinoma promoted by alcoholic liver disease. World J. Gastroenterol. *22*, 4091–4108.
10. He, X., Li, W.S., Qiu, Z.G., Zhang, L., Long, H.M., Zhang, G.S., Huang, Y.W., Zhan, Y.M., and Meng, F. (2022). A computational method for large-scale identification of esophageal cancer-related genes. Front. Oncol. *12*, 982641.
11. Liu, Z., Li, S., Huang, S., Wang, T., and Liu, Z. (2021). N(6)-Methyladenosine Regulators and Related LncRNAs Are Potential to be Prognostic Markers for Uveal Melanoma and Indicators of Tumor Microenvironment Remodeling. Front. Oncol. *11*, 704543.
12. Li, G.W., Nan, F., Yuan, G.H., Liu, C.X., Liu, X., Chen, L.L., Tian, B., and Yang, L. (2021). SCAPTURE: a deep learning-embedded pipeline that captures polyadenylation information from 3' tag-based RNA-seq of single cells. Genome Biol. *22*, 221.
13. Zhang, L., Wang, W., Wang, R., Zhang, N., Shang, H., Bi, Y., Chen, D., Zhang, C., Li, L., Yin, J., et al. (2021). Reshaping the Immune Microenvironment by Oncolytic Herpes Simplex Virus in Murine Pancreatic Ductal Adenocarcinoma. Mol. Ther. *29*, 744–761.
14. Furgiuele, S., Descamps, G., Lechien, J.R., Dequanter, D., Journe, F., and Saussez, S. (2022). Immunoscore Combining CD8, FoxP3, and CD68-Positive Cells Density and Distribution Predicts the Prognosis of Head and Neck Cancer Patients. Cells *11*, 2050.
15. Wei, Y.T., Wang, X.R., Yan, C., Huang, F., Zhang, Y., Liu, X., Wen, Z.F., Sun, X.T., Zhang, Y., Chen, Y.Q., et al. (2022). Thymosin α-1 Reverses M2 Polarization of Tumor-Associated Macrophages during Efferocytosis. Cancer Res. *82*, 1991–2002.
16. Gerlach, B.D., Ampomah, P.B., Yurdagul, A., Jr., Liu, C., Lauring, M.C., Wang, X., Kasikara, C., Kong, N., Shi, J., Tao, W., and Tabas, I. (2021). Efferocytosis induces macrophage proliferation to help resolve tissue injury. Cell Metab. *33*, 2445–2463.e8.
17. Block, S., Maier, W., Bittner, R., Büchler, M., Malfertheiner, P., and Beger, H.G. (1986). Identification of pancreas necrosis in severe acute pancreatitis: imaging procedures versus clinical staging. Gut *27*, 1035–1042.
18. Roy, S., Bag, A.K., Dutta, S., Polavaram, N.S., Islam, R., Schellenburg, S., Banwait, J., Guda, C., Ran, S., Hollingsworth, M.A., et al. (2018). Macrophage-Derived Neuropilin-2 Exhibits Novel Tumor-Promoting Functions. Cancer Res. *78*, 5600–5617.
19. Anandan, V., Thulaseedharan, T., Suresh Kumar, A., Chandran Latha, K., Revikumar, A., Mullasari, A., Kartha, C.C., Jaleel, A., and Ramachandran, S. (2021). Cyclophilin A Impairs Efferocytosis and Accelerates Atherosclerosis by Overexpressing CD 47 and Down-Regulating Calreticulin. Cells *10*, 3598.
20. Zheng, Q., Gao, N., Sun, Q., Li, X., Wang, Y., and Xiao, H. (2021). bfc, a novel serpent co-factor for the expression of croquemort, regulates efferocytosis in Drosophila melanogaster. PLoS Genet. *17*, e1009947.
21. Zhu, L., Giunzioni, I., Tavori, H., Covarrubias, R., Ding, L., Zhang, Y., Ormseth, M., Major, A.S., Stafford, J.M., Linton, M.F., and Fazio, S. (2016). Loss of Macrophage Low-Density Lipoprotein Receptor-Related Protein 1 Confers Resistance to the Antiatherogenic Effects of Tumor Necrosis Factor-α Inhibition. Arterioscler. Thromb. Vasc. Biol. *36*, 1483–1495.
22. Jiang, C., Liu, Z., Hu, R., Bo, L., Minshall, R.D., Malik, A.B., and Hu, G. (2017). Inactivation of Rab11a GTPase in Macrophages Facilitates Phagocytosis of Apoptotic Neutrophils. J. Immunol. *198*, 1660–1672.
23. Yang, A., Dai, J., Xie, Z., Colman, R.W., Wu, Q., Birge, R.B., and Wu, Y. (2014). High molecular weight kininogen binds phosphatidylserine and opsonizes urokinase plasminogen activator receptor-mediated efferocytosis. J. Immunol. *192*, 4398–4408.
24. Gronski, M.A., Kinchen, J.M., Juncadella, I.J., Franc, N.C., and Ravichandran, K.S. (2009). An essential role for calcium flux in phagocytes for apoptotic cell engulfment and the anti-inflammatory response. Cell Death Differ. *16*, 1323–1331.
25. Kim, W., Kim, H.U., Lee, H.N., Kim, S.H., Kim, C., Cha, Y.N., Joe, Y., Chung, H.T., Jang, J., Kim, K., et al. (2015). Taurine Chloramine Stimulates Efferocytosis Through Upregulation of Nrf2-Mediated Heme Oxygenase-1 Expression in Murine Macrophages: Possible Involvement of Carbon Monoxide. Antioxid. Redox Signal. *23*, 163–177.
26. Ma, L., Ma, J., Teng, M., and Li, Y. (2022). Visual Analysis of Colorectal Cancer Immunotherapy: A Bibliometric Analysis From 2012 to 2021. Front. Immunol. *13*, 843106.
27. Peng, L., Linghu, R., Chen, D., Yang, J., Kou, X., Wang, X.Z., Hu, Y., Jiang, Y.Z., and Yang, J. (2017). Inhibition of glutathione metabolism attenuates esophageal cancer progression. Exp. Mol. Med. *49*, e318.
28. Mohlin, S., Hansson, K., Radke, K., Martinez, S., Blanco-Apiricio, C., Garcia-Ruiz, C., Welinder, C., Esfandyari, J., O'Neill, M., Pastor, J., et al.

(2019). Anti-tumor effects of PIM/PI3K/mTOR triple kinase inhibitor IBL-302 in neuroblastoma. EMBO Mol. Med. *11*, e10058.

29. Li, M.Y., Fan, L.N., Han, D.H., Yu, Z., Ma, J., Liu, Y.X., Li, P.F., Zhao, D.H., Chai, J., Jiang, L., et al. (2020). Ribosomal S6 protein kinase 4 promotes radioresistance in esophageal squamous cell carcinoma. J. Clin. Investig. *130*, 4301–4319.
30. Cao, X., Cai, H., Li, N., Zheng, B., Zheng, Z., and Liu, M. (2022). First-line nivolumab plus ipilimumab or chemotherapy versus chemotherapy alone for advanced esophageal cancer: a cost-effectiveness analysis. Ther. Adv. Med. Oncol. *14*, 17588359221122733.
31. Yang, M., Hu, P., Li, M., Ding, R., Wang, Y., Pan, S., Kang, M., Kong, W., Du, D., and Wang, F. (2021). Computed Tomography-Based Radiomics in Predicting T Stage and Length of Esophageal Squamous Cell Carcinoma. Front. Oncol. *11*, 722961.
32. Tajbakhsh, A., Gheibi Hayat, S.M., Movahedpour, A., Savardashtaki, A., Loveless, R., Barreto, G.E., Teng, Y., and Sahebkar, A. (2021). The complex roles of efferocytosis in cancer development, metastasis, and treatment. Biomed. Pharmacother. *140*, 111776.
33. Liang, X., Luo, M., Shao, B., Yang, J.Y., Tong, A., Wang, R.B., Liu, Y.T., Jun, R., Liu, T., Yi, T., et al. (2022). Phosphatidylserine released from apoptotic cells in tumor induces M2-like macrophage polarization through the PSR-STAT3-JMJD3 axis. Cancer Commun. *42*, 205–222.
34. Kim, H.J., Yang, K., Kim, K., Lee, Y.J., Lee, S., Ahn, S.Y., Ahn, Y.H., and Kang, J.L. (2022). Reprogramming of cancer-associated fibroblasts by apoptotic cancer cells inhibits lung metastasis via Notch1-WISP-1 signaling. Cell. Mol. Immunol. *19*, 1373–1391.
35. Yang, M., Liu, J., Piao, C., Shao, J., and Du, J. (2015). ICAM-1 suppresses tumor metastasis by inhibiting macrophage M2 polarization through blockade of efferocytosis. Cell Death Dis. *6*, e1780.
36. Brunet, T., Radivojkov-Blagojevic, M., Lichtner, P., Kraus, V., Meitinger, T., and Wagner, M. (2020). Biallelic loss-of-function variants in RBL2 in siblings with a neurodevelopmental disorder. Ann. Clin. Transl. Neurol. *7*, 390–396.
37. Liu, Y., Zou, L., Tang, H., Li, J., Liu, H., Jiang, X., Jiang, B., Dong, Z., and Fu, W. (2022). Single-Cell Sequencing of Immune Cells in Human Aortic Dissection Tissue Provides Insights Into Immune Cell Heterogeneity. Front. Cardiovasc. Med. *9*, 791875.
38. Gui, M., Huang, S., Li, S., Chen, Y., Cheng, F., Liu, Y., Wang, J.A., Wang, Y., Guo, R., Lu, Y., et al. (2024). Integrative single-cell transcriptomic analyses reveal the cellular ontological and functional heterogeneities of primary and metastatic liver tumors. J. Transl. Med. *22*, 206.
39. Butler, A., Hoffman, P., Smibert, P., Papalexi, E., and Satija, R. (2018). Integrating single-cell transcriptomic data across different conditions, technologies, and species. Nat. Biotechnol. *36*, 411–420.
40. Zhao, Z., Ding, Y., Tran, L.J., Chai, G., and Lin, L. (2023). Innovative breakthroughs facilitated by single-cell multi-omics: manipulating natural killer cell functionality correlates with a novel subcategory of melanoma cells. Front. Immunol. *14*, 1196892.
41. Jiang, H., Yu, D., Yang, P., Guo, R., Kong, M., Gao, Y., Yu, X., Lu, X., and Fan, X. (2022). Revealing the transcriptional heterogeneity of organ-specific metastasis in human gastric cancer using single-cell RNA Sequencing. Clin. Transl. Med. *12*, e730.
42. Wu, F., Fan, J., He, Y., Xiong, A., Yu, J., Li, Y., Zhang, Y., Zhao, W., Zhou, F., Li, W., et al. (2021). Single-cell profiling of tumor heterogeneity and the microenvironment in advanced non-small cell lung cancer. Nat. Commun. *12*, 2540.
43. Zhou, Y., Yang, D., Yang, Q., Lv, X., Huang, W., Zhou, Z., Wang, Y., Zhang, Z., Yuan, T., Ding, X., et al. (2020). Single-cell RNA landscape of intratumoral heterogeneity and immunosuppressive microenvironment in advanced osteosarcoma. Nat. Commun. *11*, 6322.
44. Korsunsky, I., Millard, N., Fan, J., Slowikowski, K., Zhang, F., Wei, K., Baglaenko, Y., Brenner, M., Loh, P.R., and Raychaudhuri, S. (2019). Fast, sensitive and accurate integration of single-cell data with Harmony. Nat. Methods *16*, 1289–1296.
45. Gu, X., Cai, L., Luo, Z., Shi, L., Peng, Z., Sun, Y., and Chen, J. (2022). Identification and validation of a muscle failure index to predict prognosis and immunotherapy in lung adenocarcinoma through integrated analysis of bulk and single-cell RNA sequencing data. Front. Immunol. *13*, 1057088.
46. Zhang, L., Cui, Y., Zhou, G., Zhang, Z., and Zhang, P. (2024). Leveraging mitochondrial-programmed cell death dynamics to enhance prognostic accuracy and immunotherapy efficacy in lung adenocarcinoma. J. Immunother. Cancer *12*, e010008.
47. Saxena, V., Gao, H., Arregui, S., Zollman, A., Kamocka, M.M., Xuei, X., McGuire, P., Hutchens, M., Hato, T., Hains, D.S., and Schwaderer, A.L. (2021). Kidney intercalated cells are phagocytic and acidify internalized uropathogenic Escherichia coli. Nat. Commun. *12*, 2405.
48. Bhat-Nakshatri, P., Gao, H., Sheng, L., McGuire, P.C., Xuei, X., Wan, J., Liu, Y., Althouse, S.K., Colter, A., Sandusky, G., et al. (2021). A single-cell atlas of the healthy breast tissues reveals clinically relevant clusters of breast epithelial cells. Cell Rep. Med. *2*, 100219.
49. Piñeros, A.R., Gao, H., Wu, W., Liu, Y., Tersey, S.A., and Mirmira, R.G. (2020). Single-Cell Transcriptional Profiling of Mouse Islets Following Short-Term Obesogenic Dietary Intervention. Metabolites *10*, 513.
50. Piñeros, A.R., Kulkarni, A., Gao, H., Orr, K.S., Glenn, L., Huang, F., Liu, Y., Gannon, M., Syed, F., Wu, W., et al. (2022). Proinflammatory signaling in islet β cells propagates invasion of pathogenic immune cells in autoimmune diabetes. Cell Rep. *39*, 111011.
51. Han, D., Han, Y., Guo, W., Wei, W., Yang, S., Xiang, J., Che, J., Zhu, L., Hang, J., van den Ende, T., et al. (2023). High-dimensional single-cell proteomics analysis of esophageal squamous cell carcinoma reveals dynamic alterations of the tumor immune microenvironment after neoadjuvant therapy. J. Immunother. Cancer *11*, e007847.
52. Franken, A., Van Mol, P., Vanmassenhove, S., Donders, E., Schepers, R., Van Brussel, T., Dooms, C., Yserbyt, J., De Crem, N., Testelmans, D., et al. (2022). Single-cell transcriptomics identifies pathogenic T-helper 17.1 cells and pro-inflammatory monocytes in immune checkpoint inhibitor-related pneumonitis. J. Immunother. Cancer *10*, e005323.
53. Hatzistergos, K.E., Durante, M.A., Valasaki, K., Wanschel, A.C.B.A., Harbour, J.W., and Hare, J.M. (2020). A novel cardiomyogenic role for Isl1(+) neural crest cells in the inflow tract. Sci. Adv. *6*, eaba9950.
54. Langkabel, J., Horne, A., Bonaguro, L., Holsten, L., Hesse, T., Knaus, A., Riedel, Y., Becker, M., Händler, K., Elmzzahi, T., et al. (2021). Induction of Rosette-to-Lumen stage embryoids using reprogramming paradigms in ESCs. Nat. Commun. *12*, 7322.
55. Zhang, Q., Fei, L., Han, R., Huang, R., Wang, Y., Chen, H., Yao, B., Qiao, N., Wang, Z., Ma, Z., et al. (2022). Single-cell transcriptome reveals cellular hierarchies and guides p-EMT-targeted trial in skull base chordoma. Cell Discov. *8*, 94.
56. Alexa, A., Rahnenführer, J., and Lengauer, T. (2006). Improved scoring of functional groups from gene expression data by decorrelating GO graph structure. Bioinformatics *22*, 1600–1607.
57. Yang, L., He, Y.T., Dong, S., Wei, X.W., Chen, Z.H., Zhang, B., Chen, W.D., Yang, X.R., Wang, F., Shang, X.M., et al. (2022). Single-cell transcriptome analysis revealed a suppressive tumor immune microenvironment in EGFR mutant lung adenocarcinoma. J. Immunother. Cancer *10*, e003534.
58. Sorin, M., Karimi, E., Rezanejad, M., Yu, M.W., Desharnais, L., McDowell, S.A.C., Doré, S., Arabzadeh, A., Breton, V., Fiset, B., et al. (2023). Single-cell spatial landscape of immunotherapy response reveals mechanisms of CXCL13 enhanced antitumor immunity. J. Immunother. Cancer *11*, e005545.
59. Long, Z., Sun, C., Tang, M., Wang, Y., Ma, J., Yu, J., Wei, J., Ma, J., Wang, B., Xie, Q., and Wen, J. (2022). Single-cell multiomics analysis reveals regulatory programs in clear cell renal cell carcinoma. Cell Discov. *8*, 68.

60. Wang, J., Ren, M., Yu, J., Hu, M., Wang, X., Ma, W., Jiang, X., and Cui, J. (2022). Single-cell RNA sequencing highlights the functional role of human endogenous retroviruses in gallbladder cancer. EBioMedicine *85*, 104319.

61. Gulati, G.S., Sikandar, S.S., Wesche, D.J., Manjunath, A., Bharadwaj, A., Berger, M.J., Ilagan, F., Kuo, A.H., Hsieh, R.W., Cai, S., et al. (2020). Single-cell transcriptional diversity is a hallmark of developmental potential. Science *367*, 405–411.

62. Zheng, B., Ko, K.P., Fang, X., Wang, X., Zhang, J., Jun, S., Kim, B.J., Luo, W., Kim, M.J., Jung, Y.S., et al. (2021). A new murine esophageal organoid culture method and organoid-based model of esophageal squamous cell neoplasia. iScience *24*, 103440.

63. Nilsson, F., Storm, P., Sozzi, E., Hidalgo Gil, D., Birtele, M., Sharma, Y., Parmar, M., and Fiorenzano, A. (2021). Single-Cell Profiling of Coding and Noncoding Genes in Human Dopamine Neuron Differentiation. Cells *10*, 137.

64. Mathew, N.R., Jayanthan, J.K., Smirnov, I.V., Robinson, J.L., Axelsson, H., Nakka, S.S., Emmanouilidi, A., Czarnewski, P., Yewdell, W.T., Schön, K., et al. (2021). Single-cell BCR and transcriptome analysis after influenza infection reveals spatiotemporal dynamics of antigen-specific B cells. Cell Rep. *35*, 109286.

65. Duan, Y., and Xu, X. (2023). A signature based on anoikis-related genes for the evaluation of prognosis, immunoinfiltration, mutation, and therapeutic response in ovarian cancer. Front. Endocrinol. *14*, 1193622.

66. Zhao, K., Qian, C., Qi, L., Li, Q., Zhao, C., Zhang, J., Han, G., Xia, L., El-Bahy, Z.M., Gu, J., et al. (2024). Modified acid polysaccharide derived from Salvia przewalskii with excellent wound healing and enhanced bioactivity. Int. J. Biol. Macromol. *263*, 129803.

67. Mota, A.C., Dominguez, M., Weigert, A., Snodgrass, R.G., Namgaladze, D., and Brüne, B. (2021). Lysosome-Dependent LXR and PPARδ Activation Upon Efferocytosis in Human Macrophages. Front. Immunol. *12*, 637778.

68. Zhou, Y., Fei, M., Zhang, G., Liang, W.C., Lin, W., Wu, Y., Piskol, R., Ridgway, J., McNamara, E., Huang, H., et al. (2020). Blockade of the Phagocytic Receptor MerTK on Tumor-Associated Macrophages Enhances P2X7R-Dependent STING Activation by Tumor-Derived cGAMP. Immunity *52*, 357–373.e9.

STAR★METHODS

KEY RESOURCES TABLE

REAGENT or RESOURCE	SOURCE	IDENTIFIER
Antibodies		
Bavituximab	MCE	HY-P99279
Anti-TP63 (for ChIP, WB)	Abcam	ab238079; ab124762
Anti-RAC2 (for WB)	Abcam; Proteintech	ab154711; 60077-1-Ig
Anti-CD163 (for flow cytometry)	BioLegend; Thermo Fisher Scientific	333626; 46-1631-82
Anti-CD86 (for flow cytometry)	BioLegend	374206; 159204
Anti-F4/80 (APC-conjugated, for flow cytometry)	BioLegend	123116
Anti-CD11b (PE-conjugated, for flow cytometry)	BioLegend	982606
Anti-rabbit IgG (for WB)	Abcam	ab205718
Anti-mouse IgG (for WB)	Abcam	ab6728
Biological Samples		
Primed peripheral blood mononuclear cell	Shanghai AoNeng Biotechnology	N/A
Chemicals, Peptides, and Recombinant Proteins		
Phorbol 12-myristate-13-acetate (PMA)	MCE	HY-18739
Recombinant Human M-CSF	Peprotech	300-25-10UG
Recombinant Mouse M-CSF	Peprotech	315-02-1MG
Dexamethasone	Sigma-Aldrich	D4902
Cisplatin	MCE	HY-17394
Cell Tracker™ Green CMFDA	Yeasen	40721ES50
Lipofectamine™ RNAiMAX	Thermo Fisher Scientific	13778075
Lipofectamine™ 2000	Thermo Fisher Scientific	11668019
Critical Commercial Assays		
miRNAeasy Mini Kit	Qiagen	217084
cDNA Synthesis Kit	Takara	6210B
SYBR green qPCR reagent	Takara	RR820B
Dual-Luciferase® Reporter Assay System	Promega	E1910
Chromatin Immunoprecipitation (ChIP) Kit	Millipore	17–371
IL-10 ELISA Kit	Thermo Fisher Scientific	BMS215
TGF-β ELISA Kit	Invitrogen (Thermo)	EH449RB
TNF-α ELISA Kit	Thermo Fisher Scientific	KAC1751
Deposited data		
Raw single-cell RNA-seq data	GSA	HRA013708
Experimental Models: Cell Lines		
Human: EC9706 ESCC cell line	Mingzhoubio	MZ-1077
Human: KYSE180 ESCC cell line	Procell	CL-0760
Human: THP-1 monocyte cell line	Procell	CL-0233
Mouse: RAW264.7 macrophage cell line	Procell	CL-0190
Mouse: AKR ESCC cell line	SUNNCELL	SNL-647
Human: HEK293T cell line	Procell	CL-0005
Experimental Models: Organisms/Strains		
Mouse: BALB/c	Vital River Laboratory Co., Ltd.	N/A
Oligonucleotides		
siRNA targeting TP63	Beijing Tsingke	N/A
siRNA targeting KLF5	Beijing Tsingke	N/A

(*Continued on next page*)

Continued		
REAGENT or RESOURCE	SOURCE	IDENTIFIER
shRNA targeting mouse Tp63 (in PLKO.1 vector)	Azenta (Suzhou, China)	N/A
qPCR Primers for TP63, RAC2, *IL-10*, TGF-β, TNF-α, GAPDH	Beijing Tsingke	N/A
Software and Algorithms		
R		v4.4.1
Python		v3.7
CellRanger		v4.0.0
Seurat		v4.3.0
DoubletFinder		v2.0.3
Harmony		v0.1.1
CytoTRACE		v0.3.3
Slingshot		v2.6.0
inferCNV		v1.22.0
SCENIC		v1.3.1
DESeq2		1.46.0
clusterProfiler		4.6.2
Other		
FlowJo	BD Life Sciences	v10.8.1
Confocal microscope	Leica	N/A
Flow cytometer	BD Biosciences	N/A
Multiplex IHC Kit (AlphaTSA)	AlphaX Biotech	AXT37100041
L-929 fibroblast-conditioned media	Prepared in-lab	N/A

EXPERIMENTAL MODEL AND STUDY PARTICIPANT DETAILS

Human specimens

A cohort of patients diagnosed with ESCC based on pathological examination was recruited for this study, and none of the patients underwent preoperative treatment. A total of 27 surgically resected specimens were obtained from 9 ESCC patients, comprising 9 tumor tissues and 18 paired lymph nodes. Fresh samples were immediately subjected to scRNA-seq. All clinical samples were obtained from Ningbo Medical Center, Lihuili Hospital, and relevant clinical information is summarized in key resources table. This study adhered to all pertinent ethical regulations and was approved by the Ethics Committee of Ningbo Medical Center, Lihuili Hospital. Written informed consent was obtained from all the participants.

Humanized PBMC mouse model

The humanized PBMC (hu-PBMC) mouse model was established by using the NOG mice (Beijing Vital River Laboratories, Beijing, China). The primed peripheral blood mononuclear cells (PBMCs) were provided by Shanghai AoNeng Biotechnology (Shanghai, China). Six-week-old female mice were transplanted with 5×10^6 PBMCs by tail intravenous injection. Quantification of the percentages of human $CD45^+$ cells in the peripheral blood was used to determine the levels of engraftment. The mice were subcutaneously injected with 2×10^6 ESCC cells in the flank. Measurements of the tumor were carried out every three days. Nine days post-inoculation, shRNA and overexpression plasmids were intraperitoneally injected into the mice every 3 days. All animal experiments were conducted in accordance with the guidelines and approval of the Institutional Animal Care and Use Committee (IACUC) of Ningbo University (Approval No. 13124).

Cell culture

Human esophageal cancer cell lines EC9706 and KYSE180, mouse esophageal cancer cell line AKR, and mouse macrophage cell line RAW264.7, were cultured in DMEM (Gibco, USA) and human macrophages THP-1 were cultured in RPMI-1640 (Gibco, USA) containing 10% fetal bovine serum (FBS; Gibco, USA) and 1% penicillin/streptomycin (Thermo, USA). All cells were maintained at 37°C in an incubator filled with 5% CO_2. All cell lines were regularly tested and confirmed to be free of mycoplasma contamination. All human and mouse cell lines (EC9706, KYSE180, THP-1, AKR, and RAW264.7) were authenticated using short tandem repeat (STR) profiling.

METHOD DETAILS

Data of single cell cource collection

scRNA-seq data were obtained from the Gene Expression Omnibus website (https://www.ncbi.nlm.nih.gov/geo/), and the GSE accession number is GSE196756.

Single cell suspensions, library construction, and sequencing

Clinical samples were promptly collected following surgical procedures and single-cell suspensions were generated through mechanical dissociation and enzymatic digestion. The concentrations of single-cell suspensions were adjusted accordingly. Subsequently, the Chromium Single Cell 3′ Library & Gel Bead Kit v2 (PN-120237), Chromium Single Cell 3′ Chip Kit v2 (PN-120236), and Chromium i7 Multiplex Kit (PN-120262) were employed in accordance with the manufacturer's instructions. All subsequent steps were carried out according to established manufacturer's protocols. The completed libraries were sequenced using an Illumina NovaSeq6000 system.[36,37]

Single-Cell RNA-Seq data processing

The CellRanger-4.0.0 package was used in conjunction with the "cellranger mkfastq" function to generate raw FASTQs. Subsequently, the raw FASTQ files were aligned to the human reference genome, filtered, and underwent barcode counting and unique molecular identifier counting to produce single-cell gene expression profiles, using the "cellranger count" function.[38] To mitigate any potential bias, the "cellranger aggr" function was employed to aggregate the gene expression counts obtained from the "cellranger count" function across all samples, thereby normalizing these counts to a consistent sequencing depth and recalculating the feature-barcode single-cell gene expression matrices.

The raw gene expression data were imported into R software (version 4.4.1) for analysis using the Seurat R package (version 4.3.0).[39] Quality control was conducted using the DoubletFinder R package (version 2.0.3)[40] with the following thresholds: (1) 300 < nFeature <7,500; (2) 500 < nCount <100,000; (3) mitochondrial gene expression not exceeding 25% of the total number of genes in the cell; and (4) erythroid gene expression not exceeding 5% of the total number of genes in the cell.

Gene expression matrices for the cells were generated using logarithmic normalization and linear regression techniques by utilizing the "NormalizeData" and "ScaleData" functions.[41] The "FindVariable" function[42] was applied to identify the top 2,000 most variable genes. To mitigate batch effects, the harmony package (version 0.1.1) was used, and the first 30 principal components were selected for further analysis.[43,44] The top 30 principal components were used as input for the "FindClusters" function, resulting in the identification of different cell clusters.[45,46]

Determination of cell subtypes

Cell clusters were initially identified using the "FindClusters" and "FindNeighbors" functions implemented in Seurat.[47–50] The clusters were then annotated based on the average gene expression of the canonical markers.[51,52] To determine marker genes for each sub-cluster within the major cell types, the "FindAllMarkers" function in Seurat was used. This function utilizes a two-sided nonparametric Wilcoxon rank-sum test to compare the expression levels of all genes between different subclusters.[53,54] The parameters min. pct and min.diff.pct were set to 0.25, whereas logfc. threshold was set to 0.25.[55]

Pathway enrichment analysis

Enrichment analyses of DEGs in various cell types were conducted using Gene Ontology (GO) and Gene Set Enrichment Analysis (GSEA,http://software.broadinstitute.org/gsea/msigdb)tools using ClusterProfiler R package (version 4.6.2).[56] Significance was determined for GO terms based on an adjusted $p < 0.05$.[57,58]

Identification and analysis of malignant cells with copy number variation (CNV) estimation

To distinguish malignant tumor cells from non-malignant cells, the inferCNV algorithm was employed to deduce CNV aberrations based on perturbations in chromosomal gene expression.[59,60] Endothelial cells were used as a reference, and observations were made using epithelial cells. Epithelial cells exhibiting perturbations in CNV signals were classified as malignant.

Cell stemness and developmental trajectory inference

Cellular stemness was assessed using the CytoTRACE R package (version 0.3.3),[61] which enables conjectural deduction of the temporal progression of cell differentiation. Additionally, we employed Slingshot (version 2.6.0) to unveil the trajectory of cell development, with the identified trajectories mapped onto a UMAP projection for visualization.[62–64]

Transcription factor analysis

Single-cell regulatory network inference and clustering analysis were performed using the SCENIC package (version 1.3.1) in Python (version 3.7). GRNBoost was used to identify target genes of TFs. DNA motif analysis was used to identify binding targets. AUCell analysis was used to score cell regulator activity.[40,65]

Laboratory animal culture

In all *in vivo* experiments, 6–8-week-old female mice were used. BALB/c mice were purchased from the Vital River Laboratory Co., Ltd. Mice were housed under specific pathogen-free conditions and reared on a standard 12/12-h light/dark cycle. All animal experiments complied with relevant ethical regulations and were approved by the Animal Care and Use Committee of Ningbo University.

Preparation of macrophage differentiated cells

THP-1 cells were differentiated into macrophages by 48-h incubation in a 35-mm culture dish with 40 nmol/L phorbol 12-myristate-13-acetate (PMA) followed by 24-h incubation in RPMI 1640 medium without FBS. At the end of the incubation period, the cells were washed three times with PBS to exclude undifferentiated THP-1 cells. Adherent differentiated cells were used in subsequent experiments.

Isolation of primary macrophages

The macrophages used in this study were isolated from peripheral blood mononuclear cells (PBMCs). In brief, PBMCs were placed in RPMI-1640 complete medium containing 10% (v/v) FBS, 2 mM L-glutamine, 10 U/mL penicillin,100 mg/mL streptomycin and were maintained in a 37°C incubator. After culturing for 24 h, monocytes were attached to the wall of the culture dish. The medium was then replaced with RPMI complete medium supplemented with 50 ng/mL macrophage colony stimulating factor (M-CSF) (Peprotech, USA) to stimulate the cells for 7 days. Macrophages (Mø) were used for subsequent experiments. For bone marrow-derived macrophages (BMDMs), bone marrow cells from 8 to 12-week-old mice were cultured for 7–10 days in DMEM supplemented with 10% FBS, 10 U/mL penicillin,100 mg/mL streptomycin, and 20% (vol/vol) L-929 fibroblast-conditioned media. After 4 h of adhesion on 24-well plates, the cells were rinsed, and the medium was changed to RPMI-1640 containing 10% FBS, 10 U/mL penicillin, 100 mg/mL streptomycin, and 10 ng/mL M-CSF.[66] These cells were then used for experiments after 7–10 days, when they were more than 75% confluent.

Cell transfection

The siRNAs used in this study were synthesized by Beijing Tsingke. Cell transfection was performed using Lipofectamine RNAiMAX Transfection Reagent (Thermo Fisher Scientific, USA) according to the manufacturer's protocol. Briefly, 0.1 nmol siRNA was added to 200 μL Opti-MEM (Gibco, USA) to obtain mixture A. Next, 10 μL Lipofectamine RNAiMAX diluted in 200 μL Opti-MEM was mixed with mixture A and incubated at room temperature for 20 min. Next, the RNAi duplex-Lipofectamine RNAiMAX complex was added to Mø and cultured for 8 h at 37°C. The medium was then replaced with complete culture medium and incubated for another 40 h before the subsequent experiments.

In vitro efferocytosis assay

To obtain apoptotic cells (ACs), cancer cells were placed in a 10 cm dish at a density of 5×10^6/well. After starvation for 12 h, cells were stimulated with cisplatin (10 μM) for 12 h. The next day, ACs were incubated in serum-free RPMI-1640 medium containing 2 μM Cell Tracker Green CMFDA (Cat 40721ES50, Yeasen, China) for 30 min. The medium was then discarded, and 2 mL serum-free medium was added. The ACs were collected for subsequent incubation. Mø transfected with siNC or si AKR ESCC cell line were seeded into confocal wells at a density of 10^5 cells/well. After attachment for 24 h, CMFDA-labeled ACs were added to each well at a ratio of 5:1 and incubated for 10 min at 37°C. Non-phagocytosed cells were removed, Mø were washed with PBS, and fresh culture medium was added. The cells were cultured for 3 h and observed under a confocal microscope (Leica, Germany).[67] For flow cytometry analysis, the cells were collected and centrifuged. The supernatant was discarded, and the cells were suspended in 100 μL PBS containing PE-CD11b antibody (1:100, BioLegend, USA). The cells were then incubated for 30 min at room temperature in the dark. The cells were centrifuged and resuspended in 200 μL of PBS. $CMFDA^+$/$PE\text{-}CD11b^+$ Mø cells were analyzed using a flow cytometer (BD Biosciences, USA).[68]

RNA sequencing

The wild-type and TP63-depleted human primary macrophages were co-cultured with apoptotic EC9706 cells for 2h, then unengulfed apoptotic cells were removed by washing with PBS, and the macrophages were rested in culture medium for another 2 h. Total RNA was extracted and an mRNA library was prepared using the Illumina TruSeq platform, followed by sequencing using an Illumina NextSeq 500 cartridge. Three independent experiments were performed. Rv3.2.2 was used for graphical and statistical analysis and the R package DESeq2 was used for count normalization and differential gene expression analysis of RNAseq data. We used clusterProfiler software to conduct GO functional enrichment analysis and Kyoto Encyclopedia of Genes and Genomes (KEGG) pathway enrichment analysis for differential gene sets.

Total RNA extraction, cDNA synthesis, and quantitative PCR (qPCR)

Total RNA was extracted from macrophages using the miRNAeasy Mini Kit (Qiagen, USA). cDNA was prepared using a cDNA Synthesis Kit (Takara, Japan). qPCR was performed using SYBR green reagent (Takara, Japan), according to the manufacturer's protocol.

Western blotting assay

Cells were homogenized in ice-cold RIPA lysis buffer, resolved using 12% SDS-PAGE, and transferred onto polyvinylidene fluoride membranes. After blocking with 5% non-fat milk, the membranes were probed with the following primary antibodies at 4°C overnight: TP63 (ab238079, Abcam, USA), RAC2 (ab154711, Abcam). The membranes were then incubated with anti-rabbit (ab205718, Abcam) or anti-mouse (ab6728, Abcam) antibodies at room temperature for 1 h. Images were captured after reaction with the ECL reagent (Millipore, USA).

Luciferase reporter gene assay

The potential binding sites 1 and 2/3 of TP63 on the RAC promoter region were predicted using the online tool JASPAR. The RAC2 promoter region −1405/+20 (full-length, P6), −1075/+20 (P5), −855/+20 (P4), −635/+20 (P3), −415/+20 (P2), and-305/+20 (P1) constructs were amplified from genomic DNA. Truncated RAC2 promoter constructs were cloned into pGL3-Basic and verified by sequencing. Then, THP-1 cells and human primary macrophages were transfected with siTP63 and KLF3 promoter constructs by Lipofectamine 2000, followed by dual luciferase reporter assays (Promega, Madison, WI, USA). The results are expressed as the ratio of firefly luciferase activity to Renilla luciferase activity.

Chromatin immunoprecipitation (ChIP) assay

ChIP was performed by ChIP assay kit (17–371, EZ-CHIP, Millipore) as per manufacture's protocol. Briefly, macrophages were fixed with 1% formalin, lysed, and sonicated into chromatin fragments with a length of approximately 500 bp. Then, the chromatins were incubated with anti-TP63 antibody or rabbit IgG at 4°C with rotation overnight. The next day, immunoprecipitated DNAs was purified using RNase A and proteinase K. The level of RAC2 in the purified DNA fragments was analyzed using qPCR.

In vivo efferocytosis

Apoptotic cells were labeled with cell tracker green CMFDA and injected intraperitoneally into BALB/c mice. Twenty-four hours before cell injection, mice were intraperitoneally injected with shTP63 and RAC2 overexpression vectors (GenePharma, Shanghai, China). For peritoneal macrophages, eight hours post apoptotic cell injection, the mice were sacrificed. Cold complete medium (DMEM with 10% FBS and 1% penicillin/streptomycin) was injected into the peritoneal cavity, and the peritoneal lavage was collected. The cells were centrifuged at 400 × g for 8 min and seeded in 12-well plates. Peritoneal macrophages were adhered at 37°C for 2 h, and the cells remaining in suspension were thoroughly washed away. The isolated macrophages were analyzed for protein expression using western blotting. Efferocytosis was analyzed in $CMFDA^+$ cells using flow cytometry. For macrophage polarization, cells were stained with APC-conjugated anti-F4/80 (macrophage marker), PerCP-conjugated CD163 (M2), and PE-conjugated CD86 (M1) antibodies, and analyzed by flow cytometry. All antibodies were purchased from BioLegend (USA).

In vivo thymus efferocytosis assay

Eight-week-old male mice were injected intraperitoneally with shTP63 and RAC2 overexpression vectors for 24 h, followed by an intraperitoneal injection with 250 μL PBS containing 250 μg dexamethasone (Sigma-Aldrich, USA) dissolved in DMSO. Eighteen hours after dexamethasone injection, the mice were euthanized. The thymi were harvested, mechanically disaggregated, and enumerated. Flow cytometry was performed to determine the number of Annexin V+ (Beyotime, China) and F4/80+ cells. For macrophage polarization, cells were stained with APC-conjugated anti-F4/80 (macrophage marker), PerCP-conjugated CD163 (M2) and PE-conjugated CD86 (M1) antibody and analyzed with flow cytometry. All antibodies were bought from Biolegend (USA). The PLKO.1 shTP63 plasmids were synthesized by Azenta (Suzhou, China). The PLKO.1 shTP63, psPAX2, and pMD2.G plasmids were mixed with PEI transfection reagent in opti-MEM, followed by addition in HEK293T cells. After transfection for 24 and 48 h, the culture medium that containing virus were collected and condensed. The virus titers were measured and (5 nmol/20 g body weight) were administrated intraperitoneally.

Enzyme linked immunosorbent assay (ELISA)

After the *in vivo* efferocytosis experiment, the peritoneal lavage was collected and centrifuged, and the supernatant was collected. Thymus was homogenized and centrifuged to collect the supernatant. The production of cytokines IL-10, TGF-β, and TNF-α in the supernatant was measured using an IL-10 ELISA Kit (BMS215, Thermo, USA), TGF-β ELISA Kit (EH449RB), and TNF alpha ELISA Kit (KAC1751, Thermo, USA), respectively, according to the manufacturer's protocols.

Flow cytometry

Cells were suspended in FACS staining buffer (PBS containing 2% FBS and 1 mM EDTA) at a density of 1×10^6 cells/100 μL and incubated with Fc block (anti-mouse CD16/32; BioLegend) for 30 min on ice. Cell surface immunostaining was performed using specific antibodies for 30 min on ice. The cells were then washed twice in FACS buffer and resuspended in FACS buffer for analysis on a flow cytometer (BD Bioscience, USA). For apoptosis detection, cells were washed twice with cold FACS buffer, resuspended in binding buffer, and incubated with FITC-conjugated Annexin V for 15 min at room temperature. The samples were then analyzed using a flow cytometer. Data analysis was performed using FlowJo software.

mIHC assay and image analysis

Formalin-fixed and paraffin-embedded (FFPE) tissues sectioned to 4 μm were used for histology evaluation of esophageal cancer tumors in human. For mIHC, tissue slides were deparaffinized with xylene and rehydrated through a graded series of ethanol solutions (100%, 95% and 70%). Then, slides were treated by microwave to induce antigen retrieval using citric acid solution for 15 min. For mIHC analysis of human samples, a panel of primary antibodies were used, including CD68 (1:100, ab283654, Abcam), Annexin A1 (1:1000, ab214486, Abcam), TP63(1:200, ab124762, Abcam), RAC2(1:2000,60077-1-Ig, Proteintech). Multiplex immunofluorescence staining was performed using the AlphaTSA Multiplex IHC Kit (AXT37100041, AlphaX Biotech, China). The samples were counterstained for nuclei with DAPI for 10 min and mounted in mounting medium. Multispectral images were scanned with ZEISS AXIOSCAN 7. Two specialist pathologists (blinded to the patient's information) evaluated all specimens. Based on the distinctive density and color of immunostaining in images, the percent of number and position of stained cells were quantified.

QUANTIFICATION AND STATISTICAL ANALYSIS

The analysis in this study was implemented using R and Python software. Data are expressed as the mean ± SEM of three independent replicates. Statistical significance in two or multiple groups was analyzed using Student's *t* test or one-way ANOVA using GraphPad Prism. Statistical significance was set at $p < 0.05$.